

# Direct Numerical Simulations of Three-dimensional Magnetohydrodynamic Turbulence with Random, Power-law Forcing

Ganapati Sahoo <sup>1</sup>, Nadia Bihari Padhan <sup>2</sup>, Abhik Basu <sup>3</sup>, and Rahul Pandit <sup>2,4</sup>

<sup>1</sup> Department of Mathematics and Statistics, University of Helsinki

<sup>2</sup> Centre for Condensed Matter Theory, Department of Physics, Indian Institute of Science, Bangalore 560012, India.

<sup>3</sup> Theoretical Condensed Matter Physics Division, Saha Institute of Nuclear Physics, Calcutta, India.

<sup>4</sup> Also at: Jawaharlal Nehru Centre for Advanced Scientific Research, Jakkur, Bangalore, India

E-mail: ganapati.sahoo@gmail.com; nadia@iisc.ac.in; abhik123@gmail.com; rahul@iisc.ac.in

**Abstract.** We present pseudospectral direct-numerical-simulation (DNS) studies of the three-dimensional magnetohydrodynamic (MHD) equations (3DRFMHD) with a stochastic force that has zero mean and a variance  $\sim k^{-3}$ , where  $k$  is the wavenumber, because 3DRFMHD is used in field-theoretic studies of the scaling of energy spectra in MHD turbulence. We obtain velocity and magnetic-field spectra and structure functions and, from these, the multiscaling exponent ratios  $\zeta_p/\zeta_3$ , by using the extended self similarity (ESS) procedure. These exponent ratios lie within error bars of their counterparts for conventional three-dimensional MHD turbulence (3DMHD). We then carry out a systematic comparison of the statistical properties of 3DMHD and 3DRFMHD turbulence by examining various probability distribution functions (PDFs), joint PDFs, and isosurfaces of of, e.g., the moduli of the vorticity and the current density for three magnetic Prandtl numbers  $\text{Pr}_M = 0.1, 1, \text{ and } 10$ .

PACS numbers:

## 1. Introduction

The elucidation of the statistical properties of turbulence continues to fascinate scientists [1, 2] for it poses very challenging problems, experimental, numerical, and theoretical, that lie at the interfaces between nonequilibrium statistical mechanics, the nonlinear dynamics of extended systems, and fluid dynamics. This fascination is not restricted to fluid turbulence, for which we use the Navier-Stokes equation, but it also extends to other forms of turbulence, such as that in conducting fluids, for which we use the equations of magnetohydrodynamics (MHD) [3, 4, 5, 6, 7, 8] and on which we concentrate here. The flows of such conducting fluids is often turbulent in a variety of physical settings, including liquid-metal flows in terrestrial laboratories and planetary interiors [9, 10, 11, 12, 13, 14, 15], in stars such as the sun [3, 4, 6, 7], in the solar wind [16, 17], and in the interstellar medium [4, 5, 6].

Large kinetic and magnetic Reynolds numbers,  $\text{Re} = UL/\nu$  and  $\text{Re}_M = UL/\eta$ , respectively, lead to turbulent motion of the conducting fluid; here  $L$  and  $U$  are typical length and velocity scales in the flow,  $\nu$  is the kinematic viscosity, and  $\eta$  is the magnetic diffusivity. The statistical characterization of MHD turbulence is harder than its fluid-turbulence counterpart because (a) we must control  $\text{Re}$  and  $\text{Re}_M$  and (b) we must obtain the statistical properties of both velocity and magnetic fields. Furthermore,  $\nu$  and  $\eta$  can differ by several orders of magnitude, so the magnetic Prandtl number  $\text{Pr}_M \equiv \text{Re}_M/\text{Re} = \nu/\eta$  can vary over a large range:  $\text{Pr}_M \simeq 10^{-5}$  in the liquid-sodium system [12, 13];  $\text{Pr}_M \simeq 10^{-2}$  at the base of the Sun's convection zone [18]; and  $\text{Pr}_M \simeq 10^{14}$  in the interstellar medium [19, 20]. Hence, the fluid-dissipative and magnetic-resistive scales,  $\ell_d^u$  and  $\ell_d^b$ , respectively, can be well separated in MHD turbulence:  $\ell_d^u \sim \nu^{3/4}$  and  $\ell_d^b \sim \eta^{3/4}$  at the level of Kolmogorov 1941 (K41) phenomenology [1, 21]). Careful studies of the statistical properties of MHD turbulence must resolve both these dissipative scales, a daunting task at large  $\text{Re}$ , especially if  $\text{Pr}_M$  is significantly different from unity. Most direct numerical simulations (DNS) of MHD turbulence [22, 23, 24, 25, 26, 27, 28, 29] have been restricted to  $\text{Pr}_M \simeq 1$ ; but some DNSs have now started moving away from the  $\text{Pr}_M \simeq 1$  regime [30, 31, 32, 33].

We investigate the properties of incompressible MHD turbulence in three dimensions (3D), in the absence of a mean magnetic field and with a specific type of power-law, random forcing, which we define precisely below; henceforth, we refer to this type of MHD as 3DRFMHD, as opposed to its conventionally forced counterpart, which we refer to as 3DMHD. The motivation for our study arises from the use of such random forcing for field-theoretical studies, initially of fluid turbulence [34, 35, 36, 37, 38, 39] and subsequently of MHD turbulence [8, 40, 41, 42, 43, 44, 45, 46, 47]. It is useful, therefore, to examine the statistical properties of 3DRFMHD turbulence by a careful, direct numerical simulation (DNS). Such DNS studies have been carried out, with this type of power-law, random forcing, for the one-dimensional Burgers [48, 49, 50], three-dimensional Navier-Stokes [51, 52], and two-dimensional Navier-Stokes equations [53] but not, so far, for 3DRFMHD turbulence. One of the principal goals of our study is to

investigate whether the inertial-range scaling properties of energy spectra in 3DRFMHD are the same as those of 3DMHD. We also present data for 3DRFMHD for (a) the temporal evolution of quantities such as the energy, energy-dissipation rates, Reynolds numbers, and important length scales, (b) energy, dissipation-rate, and effective-pressure spectra, (c) probability distribution functions (PDFs) of components of various fields, energy dissipation rates, and cosines of angles between various vectors, (d) velocity and magnetic-field structure functions, which can be used to characterize inertial-range intermittency, (e) isosurfaces of the moduli of the vorticity and the current, the energy-dissipation rates, and the effective pressure, and (f) joint PDFs that characterize the statistical correlation between various quantities. Field-theoretical studies have not, so far, computed as many quantities as we calculate for 3DRFMHD; thus, a comparison of our results here with those available from DNS studies of 3DMHD [32, 33] provides a guide to which statistical properties of 3DMHD might emerge from analytical but, perforce, approximate studies of 3DRFMHD. Our study examines the magnetic-Prandtl-number dependence of 3DRFMHD, by carrying out DNSs at  $\text{Pr}_M = 0.1, 1, \text{ and } 10$ . We follow the 3DMHD investigations of Ref. [32, 33], so we do not include (a) compressible MHD turbulence, (b) a mean magnetic field (as, e.g., in Ref. [54]) and (c) Lagrangian properties (see, e.g., Ref. [55]).

Such a comprehensive study of 3DRFMHD turbulence has not been attempted hitherto. Given our error bars, we find that there is agreement between our 3DRFMHD exponent ratios with those of 3DMHD [32, 33]. The  $\text{Pr}_M$  dependence of these exponent ratios is also similar for 3DRFMHD and 3DMHD turbulence. This is of importance in deciding whether 3DRFMHD can be used for obtaining universal statistical properties, such as exponent ratios, by employing field-theoretic renormalization-group methods. Although these exponent ratios for 3DRFMHD and 3DMHD seem to agree, some PDFs are different in detail and the isosurfaces mentioned above are qualitatively different. Furthermore, strictly speaking (see below), 3DMHD and 3DRFMHD turbulence cannot be in the same universality class because of logarithmic corrections to, say, the energy spectrum because of the power law in the random forcing we employ (for a discussion in the analogous randomly forced versions of the 3D Navier-Stokes equation and the 1D Burgers equation see Refs. [50, 51]).

We organize the remaining part of this paper as follows: In Sec. 2 we describe the 3DRFMHD equations, the forcing method and the numerical scheme we use, and the statistical measures we employ to characterize 3DRFMHD turbulence. In Sec. 3 we present our results in several subsections: Subsection 3.1 is devoted to the temporal evolution of quantities such as the energy and energy-dissipation rates, Reynolds number, and important length scales; in Subsec. 3.2 we present energy, dissipation-rate, and effective-pressure spectra; in Subsec. 3.3 we show probability distribution functions (PDFs) of quantities such as components of fields, energy-dissipation rates, and cosines of angles between various vectors; in Subsec. 3.4 we present velocity and magnetic-field structure functions and explain how they can be used to characterize inertial-range intermittency; in Subsec. 3.5 we display the isosurfaces mentioned above;

in Subsec. 3.6 we present joint PDFs that quantify the statistical correlation between various quantities. Section 4 contains a discussion of our results.

## 2. Equations, Numerical Methods, and Statistical Measures

The 3DRFMHD model is defined by the following set of equations:

$$\frac{\partial \mathbf{u}}{\partial t} + (\mathbf{u} \cdot \nabla) \mathbf{u} = \nu \nabla^2 \mathbf{u} - \nabla \bar{p} + (\mathbf{b} \cdot \nabla) \mathbf{b} + \mathbf{f}_u, \quad (1)$$

$$\frac{\partial \mathbf{b}}{\partial t} + (\mathbf{u} \cdot \nabla) \mathbf{b} = (\mathbf{b} \cdot \nabla) \mathbf{u} + \eta \nabla^2 \mathbf{b} + \mathbf{f}_b; \quad (2)$$

$\mathbf{u}$ ,  $\mathbf{b}$ ,  $\boldsymbol{\omega} = \nabla \times \mathbf{u}$  and  $\mathbf{j} = \nabla \times \mathbf{b}$  are, respectively, the velocity field, the magnetic field, the vorticity, and the current density at the point  $\mathbf{x}$  and time  $t$ ;  $\nu$  and  $\eta$  are the kinematic viscosity and the magnetic diffusivity, respectively, and the effective pressure is  $\bar{p} = p + (b^2/8\pi)$ , where  $p$  is the pressure. We enforce the incompressibility constraint

$$\nabla \cdot \mathbf{u} = 0; \quad (3)$$

and, of course,

$$\nabla \cdot \mathbf{b} = 0. \quad (4)$$

The external forces  $\mathbf{f}_u$  and  $\mathbf{f}_b$  are zero-mean, Gaussian random forces that are uncorrelated with each other and delta correlated in time; their statistical properties are best described by their covariances in Fourier space:

$$\begin{aligned} \langle \hat{f}_{u,m}(\mathbf{k}, t) \hat{f}_{u,n}(\mathbf{k}', t') \rangle &= 2D_u k^{-3} \mathcal{P}_{m,n}(\mathbf{k}) \delta(\mathbf{k} + \mathbf{k}') \delta(t - t'); \\ \langle \hat{f}_{b,m}(\mathbf{k}, t) \hat{f}_{b,n}(\mathbf{k}', t') \rangle &= 2D_b k^{-3} \mathcal{P}_{m,n}(\mathbf{k}) \delta(\mathbf{k} + \mathbf{k}') \delta(t - t'); \end{aligned} \quad (5)$$

here carets denote spatial Fourier transforms,  $\mathbf{k}$  and  $\mathbf{k}'$  are wave vectors,  $k = |\mathbf{k}|$ , the transverse projector  $\mathcal{P}_{m,n} \equiv [\delta_{m,n} - (k_m k_n / k^2)]$  ensures that  $\nabla \cdot \mathbf{u} = 0$  and  $\nabla \cdot \mathbf{b} = 0$ , and  $D_u$  and  $D_b$  are measures of the kinetic and magnetic energy injections [40]; we do not consider cross correlations between  $\mathbf{f}_u$  and  $\mathbf{f}_b$  here; and we set  $D_u = D_b$ . At the level of our DNS this stochastic forcing is generated by using the following:

$$\begin{aligned} \hat{f}_u(k_x, t) &= f_x^u e^{i\xi}; \quad \hat{f}_u(k_y, t) = f_y^u e^{i\xi}; \quad \hat{f}_u(k_z, t) = f_z^u e^{i\xi}; \\ \hat{f}_b(k_x, t) &= f_x^b e^{i\xi}; \quad \hat{f}_b(k_y, t) = f_y^b e^{i\xi}; \quad \hat{f}_b(k_z, t) = f_z^b e^{i\xi}. \end{aligned} \quad (6)$$

We choose the amplitudes of the isotropic forces as follows:

$$\begin{aligned} f_x^u &= f_{amp}^u \sin \theta \cos \phi; \quad f_y^u = f_{amp}^u \sin \theta \cos \phi; \quad f_z^u = f_{amp}^u \cos \theta; \\ f_x^b &= f_{amp}^b \sin \theta \cos \phi; \quad f_y^b = f_{amp}^b \sin \theta \cos \phi; \quad f_z^b = f_{amp}^b \cos \theta; \end{aligned} \quad (7)$$

the amplitudes are

$$\begin{aligned} f_{amp}^u &= f_{ran}^u k^{-3/2}, \\ f_{amp}^b &= f_{ran}^b k^{-3/2}, \end{aligned} \quad (8)$$

where  $f_{ran}^u$  and  $f_{ran}^b$  are Gaussian random numbers. The angles  $\xi$  and  $\theta$  are random numbers distributed uniformly in the interval  $[-\pi, \pi)$  and the angle  $\phi$  is a random

number distributed uniformly in the interval  $[0, \pi/2)$ . We use a standard pseudospectral method [32, 33, 56] to solve Eqs. 3, 4 and 5, the 2/3 rule for removing aliasing errors [56], and an Adams-Bashforth method, with step size  $\delta t$ , for time marching [32, 33].

In our DNSs we use initial (superscript 0) energy spectra  $E_u^0(k)$  and  $E_b^0(k)$ , for the velocity and magnetic fields, respectively, as in Ref. [32, 33]:

$$E_u^0(k) = E_b^0(k) = E^0 k^4 \exp(-2k^2); \quad (9)$$

the initial phases of the Fourier components of the velocity and magnetic fields are different and are chosen such that they are distributed uniformly between 0 and  $2\pi$ .

We have carried out three DNSs, each with  $512^3$  collocation points, with the following three sets of parameters:

- (i)  $\nu = 10^{-4}$ ,  $\eta = 10^{-3}$ ,  $\text{Pr}_M = 0.1$ ,  $\text{Re}_\lambda \simeq 200$ ;
- (ii)  $\nu = 10^{-3}$ ,  $\eta = 10^{-3}$ ,  $\text{Pr}_M = 1$ ,  $\text{Re}_\lambda \simeq 50$ ;
- (iii)  $\nu = 10^{-3}$ ,  $\eta = 10^{-4}$ ,  $\text{Pr}_M = 10$ ,  $\text{Re}_\lambda \simeq 40$ ;

here,  $\text{Re}_\lambda$  denotes the Taylor-microscale Reynolds number (see below) that we obtain in the statistically steady turbulent state, which is eventually established because of the stochastic forcing in the 3DRFMHD model. We then average the quantities of interest, which are described below, over 15 velocity- and magnetic-fields configurations that are well-separated in time.

### 2.1. Statistical measures

To enable a detailed comparison of our results for 3DRFMHD with their counterparts for 3DMHD, we use the same statistical, measures to characterize homogeneous, isotropic 3DRFMHD turbulence, that are employed in Ref. [32, 33]:

- The kinetic, magnetic, and total energy spectra  $E_u(k) = \sum_{\mathbf{k} \ni |\mathbf{k}|=k} |\tilde{\mathbf{u}}(\mathbf{k})|^2$ ,  $E_b(k) = \sum_{\mathbf{k} \ni |\mathbf{k}|=k} |\tilde{\mathbf{b}}(\mathbf{k})|^2$ , and  $E_T(k) = E_u(k) + E_b(k)$ , respectively.
- The kinetic, magnetic, and total energies  $E_u = \sum_k E_u(k)/2$ ,  $E_b = \sum_k E_b(k)/2$ , and  $E_T = E_u + E_b$ .
- Spectra for the energy dissipation rates and the effective pressure  $\epsilon_u(k) = \nu k^2 E_u(k)$ ,  $\epsilon_b(k) = \nu k^2 E_b(k)$ , and  $P(k) = \sum_{\mathbf{k} \ni |\mathbf{k}|=k} |\tilde{p}(\mathbf{k})|^2$ , respectively.
- The Taylor-microscale Reynolds number  $\text{Re}_\lambda = u_{\text{rms}} \lambda / \nu$ , the magnetic Taylor-microscale Reynolds number  $\text{Re}_M = u_{\text{rms}} \lambda / \eta$ , and the magnetic Prandtl number  $\text{Pr}_M = \text{Re}_M / \text{Re} = \nu / \eta$ , where the root-mean-square velocity  $u_{\text{rms}} = \sqrt{2E_u/3}$  and the Taylor microscale  $\lambda = [\sum_k k^2 E(k) / E]^{-1/2}$ .
- The integral length scale  $\ell_I = [\sum_k E(k) / k] / E$ .
- The mean kinetic energy dissipation rate per unit mass,  $\epsilon_u = \nu \sum_{i,j} (\partial_i u_j + \partial_j u_i)^2 = \nu \sum_k k^2 E_u(k)$ , the mean magnetic energy dissipation rate per unit mass  $\epsilon_b = \eta \sum_{i,j} (\partial_i b_j + \partial_j b_i)^2 = \eta \sum_k k^2 E_b(k)$ , and the mean energy dissipation rate per unit mass  $\epsilon = \epsilon_u + \epsilon_b$ .

- The dissipation length scales for velocity and magnetic fields  $\eta_d^u = (\nu^3/\epsilon_u)^{1/4}$  and  $\eta_d^b = (\eta^3/\epsilon_b)^{1/4}$ , respectively. (In all our runs,  $k_{\max}\eta_d^u \gtrsim 1$  and  $k_{\max}\eta_d^b \gtrsim 1$ , where  $k_{\max}$  is the largest wave-vector magnitude allowed by the 2/3 dealiasing rule.)
- The eigenvalues  $\Lambda_n^u$  and the associated eigenvectors  $\hat{e}_n^u$ , with  $n = 1, 2, \text{ or } 3$ , of the rate-of-strain tensor  $\mathbb{S}$ , with components  $S_{ij} = \partial_i u_j + \partial_j u_i$ ; incompressibility implies  $\sum_n \Lambda_n^u = 0$ , so at least one of the  $\Lambda_n^u$  must be positive and another negative; we label them such that  $\Lambda_1^u > 0$ ,  $\Lambda_3^u < 0$ , and  $\Lambda_2^u$ , which can be positive or negative, lies in between them.
- Probability distribution functions (PDFs): PDFs of  $\Lambda_n^u$  and of the cosines of the angles that the associated eigenvectors make with the vorticity, the current density  $\mathbf{j} = \nabla \times \mathbf{b}/4\pi$ , etc. (These PDFs and those of the local cross helicity  $H_C = \mathbf{u} \cdot \mathbf{b}$  quantify the degree of alignment of pairs of vectors such as  $\mathbf{u}$  and  $\mathbf{b}$ .)
- Joint PDFs (JPDFs): We obtain the velocity-derivative tensor  $\mathbb{A}$ , with components  $A_{ij} = \partial_i u_j$  and thence the invariants  $Q = -\frac{1}{2}\text{tr}(\mathbb{A}^2)$  and  $R = -\frac{1}{3}\text{tr}(\mathbb{A}^3)$  [57], which are used to characterize fluid turbulence [57, 58, 59]. The zero-discriminant curve  $D \equiv \frac{27}{4}R^2 + Q^3 = 0$  and the  $Q$  and  $R$  axes divide the  $Q$ - $R$  plane into different four regimes:
  - $Q$  large and negative; vortex formation is not favored because local strains are high; also, if  $R > 0$  ( $R < 0$ ), fluid elements experience axial (biaxial) strain.
  - $Q$  large and positive: the flow is predominantly vortical; if, in addition,  $R > 0$  ( $R < 0$ ), vortices are stretched (compressed).
- For turbulent fluid flow, contour plots of the JPDF of  $Q$  and  $R$  (often called  $QR$  plots) exhibit a tear-drop shape. We explore these JPDFs and others, e.g., JPDFs of  $\epsilon_u$  and  $\epsilon_b$ , for 3DRFMHD turbulence.
- Structure functions: We calculate the order- $p$ , longitudinal structure functions  $S_p^a(l) \equiv \langle |\delta a_{\parallel}(\mathbf{x}, l)|^p \rangle$ ; the increment of the longitudinal component of the field  $\mathbf{a}$  is  $\delta a_{\parallel}(\mathbf{x}, l) \equiv \mathbf{a}(\mathbf{x} + \mathbf{l}, t) - \mathbf{a}(\mathbf{x}, t) \cdot \frac{\mathbf{l}}{l}$ ; here,  $\mathbf{a}$  can be  $\mathbf{u}$  or  $\mathbf{b}$ ; we also compute the hyperflatness  $F_6^a(l) = S_6^a(l)/[S_2^a(l)]^3$ .
- Intermittency: For separations  $l$  in the inertial range,  $\eta_d^u, \eta_d^b \ll l \ll L$ , we anticipate that  $S_p^a(l) \sim l^{\zeta_p^a}$ , with  $\zeta_p^a$  the multiscaling exponents for  $\mathbf{a}$ ; the Kolmogorov phenomenology (K41) of 1941 [1, 21, 27] yields  $\zeta_p^{aK41} = p/3$ ; but multiscaling corrections are substantial, with  $\zeta_p^a \neq \zeta_p^{aK41}$ , especially for  $p \geq 3$  [see Subsec. 3.4].
- We also explore the dependence on  $l$  of the PDFs of the increments  $\delta a_{\parallel}(\mathbf{x}, l)$ .

### 3. Results

We now present the results of our DNSs for 3DRFMHD with  $\text{Pr}_M = 0.1$ ,  $\text{Pr}_M = 1$ , and  $\text{Pr}_M = 10$ ; we also compare these results with their counterparts for 3DMHD [32, 33]. Subsection 3.1 gives the temporal evolution of the energy, energy-dissipation rates, the Taylor-microscale Reynolds number, the Taylor microscale, and the integral length scale; in subsection 3.2 we present energy, dissipation-rate, and effective-pressure spectra;

subsection 3.3 is devoted to probability distribution functions (PDFs) of quantities such as components of fields, energy dissipation rates and cosines of angles between various vectors; in subsection 3.4 we present velocity and magnetic-field structure functions and explain how they can be used to characterize inertial-range intermittency; subsection 3.5 displays isosurfaces mentioned above; in subsection 3.6 we present joint PDFs that give statistical correlation between various quantities.

### 3.1. Temporal evolution

Figures 1 (a), (b), and (c) show plots of the total energy  $E$  (red line), the total kinetic energy  $E_u$  (green line), and the total magnetic energy  $E_b$  (blue line) versus time  $t$  for  $\text{Pr}_M = 0.1$ ,  $\text{Pr}_M = 1$ , and  $\text{Pr}_M = 10$ , respectively; these plots are more noisy than their analogues for statistically steady 3DMHD (cf. Fig. 7 (b.1), (c.1), and (d.1) in Ref. [32]). Eventually, a statistically steady state is obtained, even for 3DRFMHD, in which  $E$ ,  $E_u$ , and  $E_b$  fluctuate about their mean values  $\langle E \rangle$ ,  $\langle E_u \rangle$ , and  $\langle E_b \rangle$ .

In Figs. 2 (a), (b), and (c) we show plots of the total energy dissipation rate  $\epsilon$  (red line), the kinetic-energy dissipation rate  $\epsilon_u$  (green line), and the magnetic-energy dissipation rate  $\epsilon_b$  (blue line) versus  $t$  for  $\text{Pr}_M = 0.1$ ,  $\text{Pr}_M = 1$ , and  $\text{Pr}_M = 10$ , respectively. The difference between the mean values of the kinetic- and magnetic-energy dissipation rates ( $\langle \epsilon_u \rangle - \langle \epsilon_b \rangle$ ) is negative at  $\text{Pr}_M = 0.1$ , it increases when  $\text{Pr}_M = 1$ , and it finally becomes positive for  $\text{Pr}_M = 10$  as we expect; this also occurs in 3DMHD (cf. Fig. 7 (b.2), (c.2), and (d.2) in Ref. [32]).

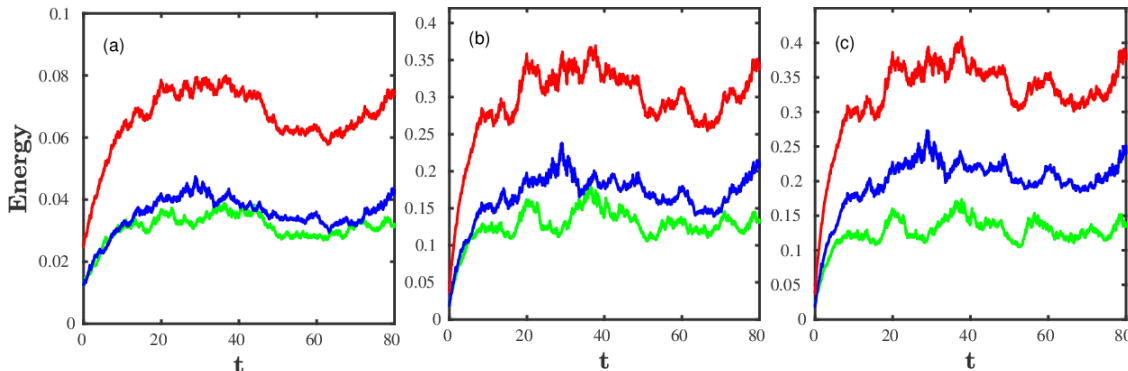


**Figure 1.** Plots of the total energy (red line), kinetic energy (green line), and magnetic energy (blue line) versus time  $t$  (product of number of steps and  $\delta t$ ) for (a)  $\text{Pr}_M = 0.1$ , (b)  $\text{Pr}_M = 1$ , and (c)  $\text{Pr}_M = 10$  (cf. Fig. 7 (b.1), (c.1), and (d.1) in Ref. [32])

Figures 3, 4, 5 show the temporal evolution of the Taylor-microscale Reynolds number  $\text{Re}_\lambda$ , the integral scale  $\ell_I$ , and the Taylor microscale  $\lambda$ , respectively, for (a)  $\text{Pr}_M = 0.1$ , (b)  $\text{Pr}_M = 1$ , and (c)  $\text{Pr}_M = 10$ . Once the statistically steady state is achieved, these quantities fluctuate about a mean. The mean value of  $\text{Re}_\lambda$  decreases with increasing  $\text{Pr}_M$ , because we force velocity and magnetic fields with equal intensity. The mean values of  $\ell_I$  and  $\lambda$  do not depend very sensitively on  $\text{Pr}_M$ .

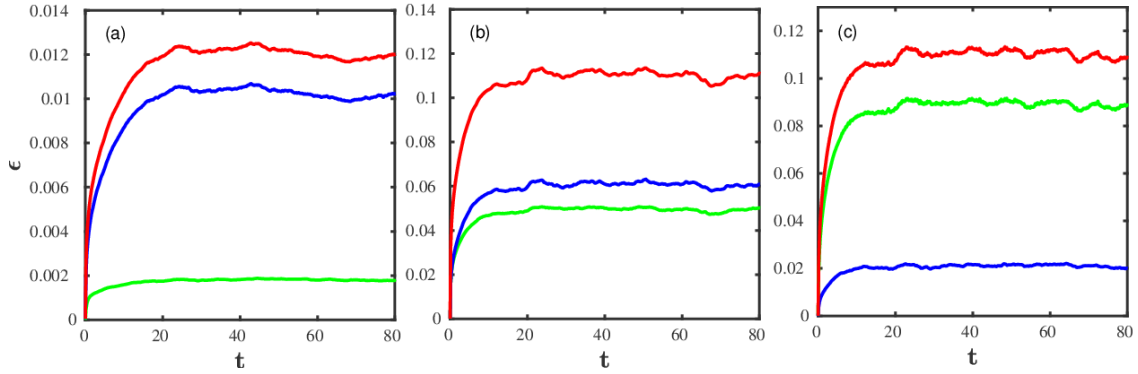


**Figure 2.** Plots of the total energy dissipation (red line), kinetic-energy dissipation (green line) and magnetic-energy dissipation (blue line) rates versus time  $t$  (product of number of steps and  $\delta t$ ) for (a)  $Pr_M = 0.1$ , (b)  $Pr_M = 1$ , and (c)  $Pr_M = 10$  (cf. Fig. 7 (b.2), (c.2), and (d.2) in Ref. [32])

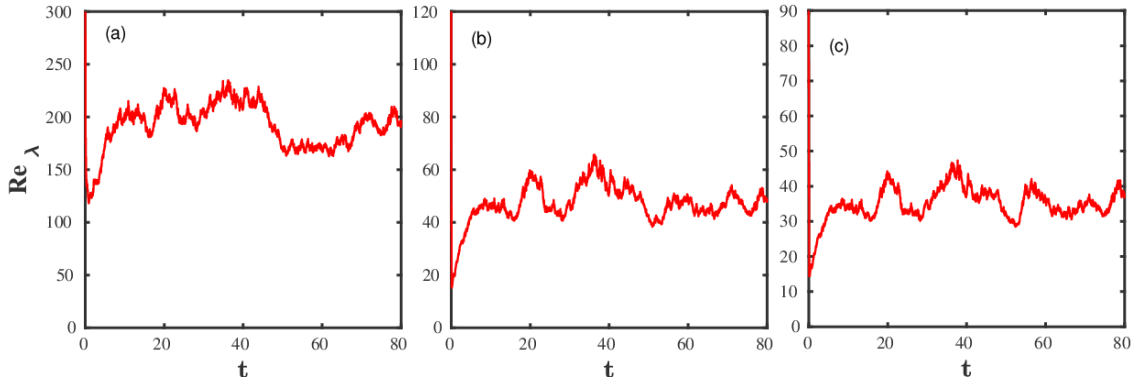


**Figure 3.** Plots of the Taylor-microscale Reynolds number  $Re_\lambda$  versus time  $t$  (product of number of steps and  $\delta t$ ) for (a)  $Pr_M = 0.1$ , (b)  $Pr_M = 1$ , and (c)  $Pr_M = 10$ .

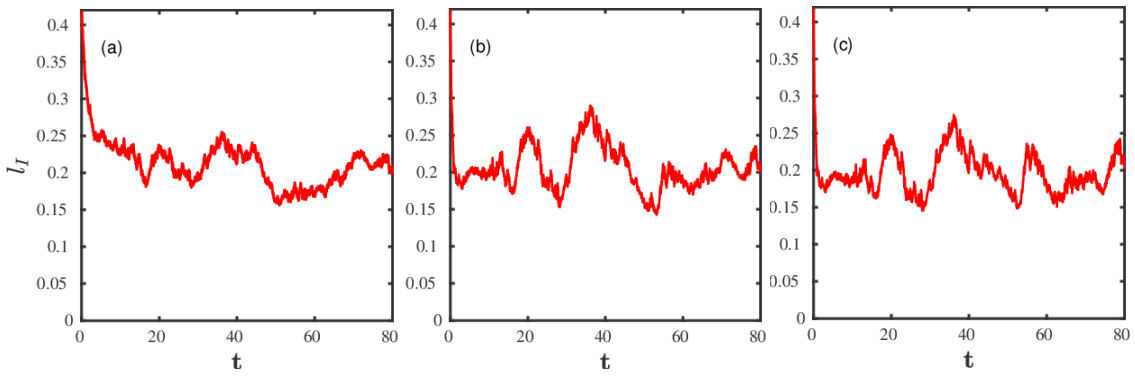


**Figure 4.** Plots of the integral scale  $l_I$  versus time  $t$  (product of number of steps and  $\delta t$ ) for (a)  $Pr_M = 0.1$ , (b)  $Pr_M = 1$ , and (c)  $Pr_M = 10$ .



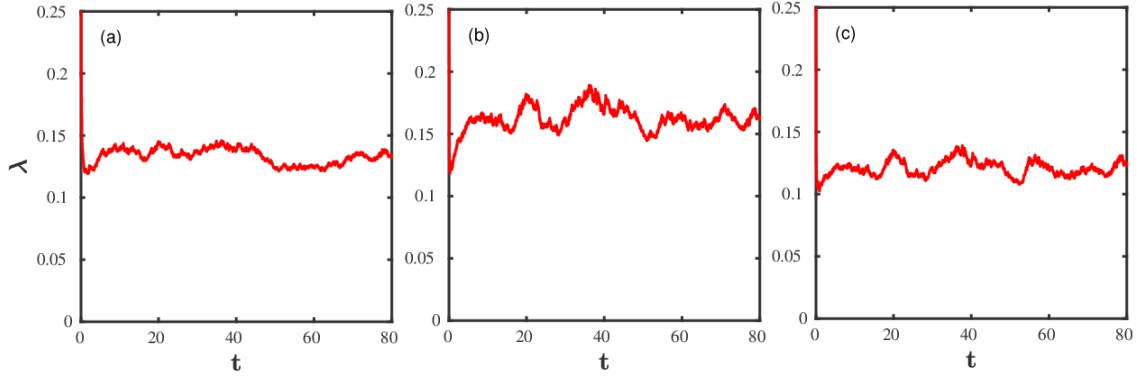


**Figure 5.** Plots of the Taylor microscale  $\lambda$  versus time  $t$  (product of number of steps and  $\delta t$ ) for (a)  $\text{Pr}_M = 0.1$ , (b)  $\text{Pr}_M = 1$ , and (c)  $\text{Pr}_M = 10$ .

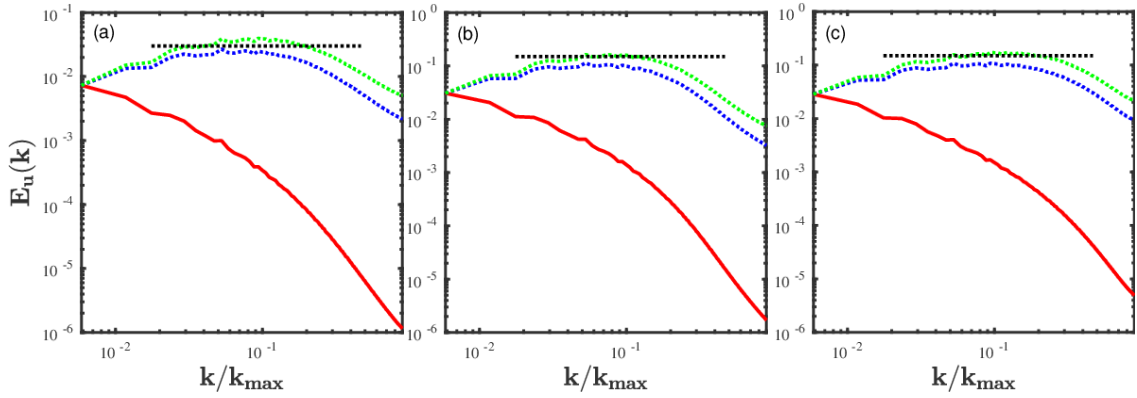


**Figure 6.** Log-log (base 10) plots of kinetic energy spectra  $E_u(k)$  (red full line), with  $k$ , the magnitude of the wave vector and the corresponding compensated spectra  $k^{5/3}E_u(k)$  (green dashed lines) and  $k^{3/2}E_u(k)$  (blue dashed lines) for (a)  $\text{Pr}_M = 0.1$ , (b)  $\text{Pr}_M = 1$ , and (c)  $\text{Pr}_M = 10$  (cf. Figs. 8 (b.3), (c.3), and (d.3) in Ref. [32])

### 3.2. Spectra

Figures 6 (a), (b), and (c) show plots of the kinetic-energy spectra  $E_u(k)$  (red full line), and the corresponding compensated spectra  $k^{5/3}E_u(k)$  (green dashed line) and  $k^{3/2}E_u(k)$  (blue dashed line) for  $\text{Pr}_M = 0.1$ ,  $\text{Pr}_M = 1$ , and  $\text{Pr}_M = 10$ , respectively; figures 7 (a), (b), and (c) show plots of the magnetic energy spectra  $E_b(k)$  (red full line), and the corresponding compensated spectra  $k^{5/3}E_b(k)$  (green dashed line) and  $k^{3/2}E_b(k)$  (blue dashed line) for  $\text{Pr}_M = 0.1$ ,  $\text{Pr}_M = 1$ , and  $\text{Pr}_M = 10$ , respectively, for 3DRFMHD. For  $\text{Pr}_M = 1$ , both kinetic- and magnetic-energy spectra have comparable inertial ranges; the former shows a larger (smaller) dissipation range than the latter as the magnetic Prandtl number increases (decreases) to  $\text{Pr}_M = 10$  (to  $\text{Pr}_M = 0.1$ ). These results are consistent the inertial-range behaviors of energy spectra in 3DMHD (cf. Figs. 8 (b.3), (c.3), and (d.3) in Ref. [32]).

Note that, because of our power-law forcing, these energy spectra for 3DRFMHD

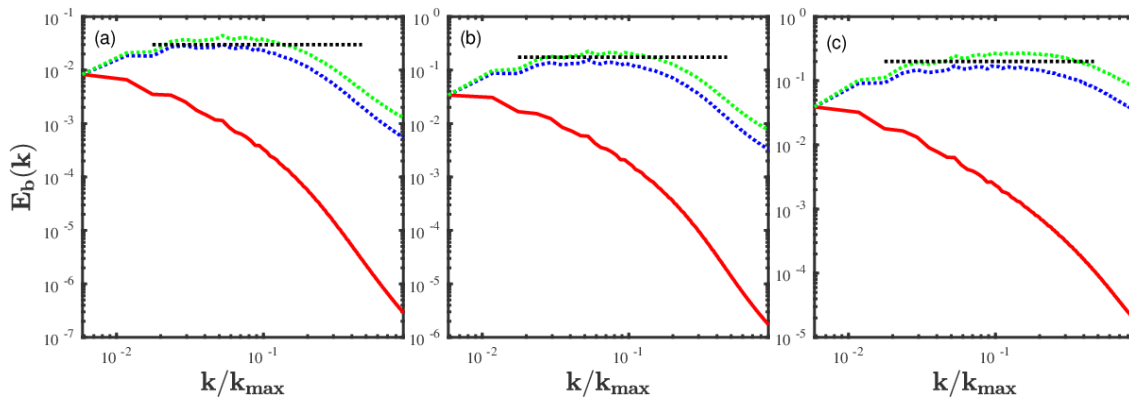


**Figure 7.** Log-log (base 10) plots of effective magnetic energy spectra  $E_b(k)$  (red full lines), with  $k$ , the magnitude of the wave vector and the corresponding compensated spectra  $k^{5/3}E_b(k)$  (green dashed lines) and  $k^{3/2}E_b(k)$  (blue dashed lines) for (a)  $\text{Pr}_M = 0.1$ , (b)  $\text{Pr}_M = 1$ , and (c)  $\text{Pr}_M = 10$  (cf. Figs. 8 (b.3), (c.3), and (d.3) in Ref. [32]).

fall more slowly in the dissipation range than their counterparts in 3DMHD; the latter decay as  $k^\gamma \exp(-\delta k)$  in the deep dissipation range [32, 33]; such an exponential decay can be obtained for 3DRFMHD, and other randomly forced models with such forcing [50, 51, 52], only if we introduce an ultraviolet cutoff for  $k$  in the forcing term. Furthermore, for 3DRFMHD we expect mild logarithmic corrections to the inertial-range, power-law forms of these spectra in 3DMHD as argued, e.g., for the analogous 3D Navier-Stokes [51] and 1D Burgers [50] equations with power-law, random forcing; such subtle logarithmic corrections cannot be uncovered reliably given the spatial resolution of our 3DRFMHD runs. These comments also apply to the inertial- and dissipation-range forms of the other spectra we discuss below.

In figures 8 (a), (b), and (c) we present the energy-dissipation spectra for the velocity (red lines) and magnetic (blue lines) fields for  $\text{Pr}_M = 0.1$ ,  $\text{Pr}_M = 1$ , and  $\text{Pr}_M = 10$ , respectively. These spectra have maxima, as in 3DMHD (cf. Figs. 10 (b.3), (c.3), and (d.3) in Ref. [32]), at the value of  $k$  at which the dissipation becomes significant and the dissipation range sets in; given that we have such maxima in all our dissipation spectra, we conclude that we have resolved both fluid and magnetic dissipation ranges adequately for all the values of  $\text{Pr}_M$  that we use.

Spectra for the effective pressure  $P(k)$  (red full lines) and their compensated versions  $k^{7/3}P(k)$  (blue dashed lines) are shown in figures 9 (a), (b), and (c) for  $\text{Pr}_M = 0.1$ ,  $\text{Pr}_M = 1$ , and  $\text{Pr}_M = 10$ , respectively. The compensated spectra show that, for all our runs, the inertial-range behaviors of these effective-pressure spectra are consistent with the K41 power law  $k^{-7/3}$  that goes with the  $k^{-5/3}$  behaviors of the energy spectra discussed above (cf. Figs. 12 (b.2), (c.2), and (d.2), for 3DMHD, in Ref. [32]).

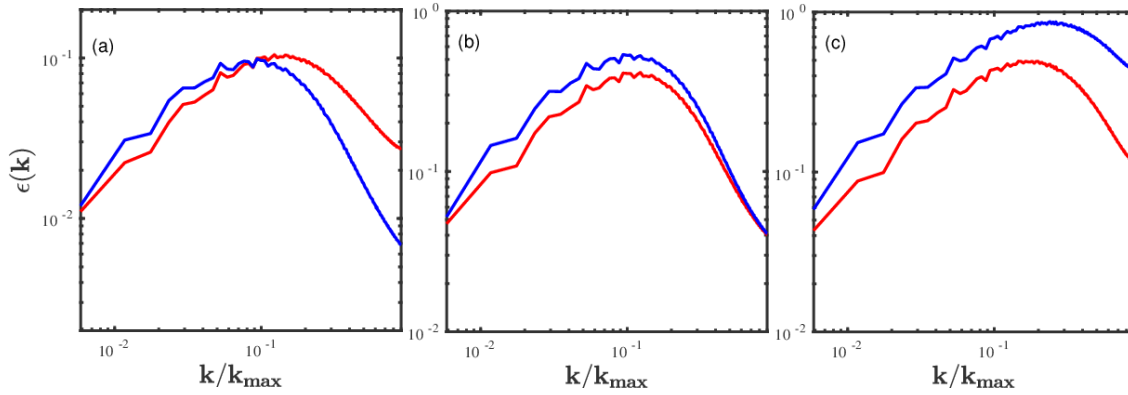


**Figure 8.** Log-log (base 10) plots of energy-dissipation spectra for the velocity (red lines) and magnetic (blue lines) fields, with  $k$  the magnitude of the wave vector for (a)  $\text{Pr}_M = 0.1$ , (b)  $\text{Pr}_M = 1$ , and (c)  $\text{Pr}_M = 10$  (cf. Figs. 10 (b.3), (c.3), and (d.3) in Ref. [32]).

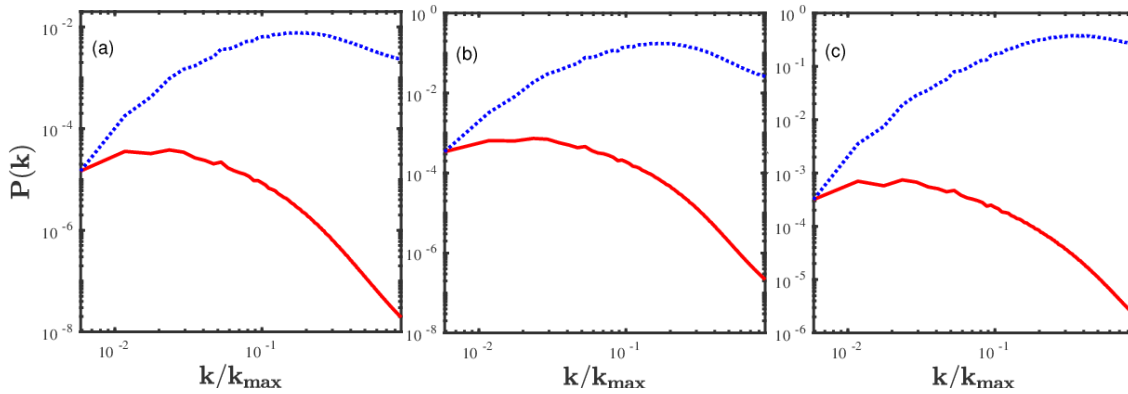


**Figure 9.** Log-log (base 10) plots of effective pressure spectra  $P(k)$  (red full lines), with  $k$  the magnitude of the wave vector and the corresponding compensated spectra  $k^{7/3}P(k)$  (blue dashed lines) for (a)  $\text{Pr}_M = 0.1$ , (b)  $\text{Pr}_M = 1$ , and (c)  $\text{Pr}_M = 10$  (cf. Figs. 12 (b.2), (c.2), and (d.2) in Ref. [32]).

### 3.3. Probability distribution functions

In this subsection we use the results of our DNS studies, for  $\text{Pr}_M = 0.1$ ,  $\text{Pr}_M = 1$ , and  $\text{Pr}_M = 10$ , to obtain several probability distribution functions (PDFs) that characterize the statistical properties of 3DRFMHD turbulence; we also compare them with their 3DMHD counterparts in Ref. [32].

Probability distribution functions of the modulus of the local cross helicity  $H_C = \mathbf{u} \cdot \mathbf{b}$  are shown in figures 10 (a), (b), and (c) for  $\text{Pr}_M = 0.1$ ,  $\text{Pr}_M = 1$ , and  $\text{Pr}_M = 10$ , respectively; the arguments of these PDFs are scaled by their root-mean-square values. For all the values of  $\text{Pr}_M$  that we consider, these PDFs are (a) peaked very close to the mean value  $\mu_{H_C} \simeq 0$ , (b) distinctly non-Gaussian, and (c) negatively skewed. The mean  $\mu_{H_C}$ , standard deviation  $\sigma_{H_C}$ , skewness  $\gamma_{3,H_C}$ , and kurtosis  $\gamma_{4,H_C}$  of the cross helicity

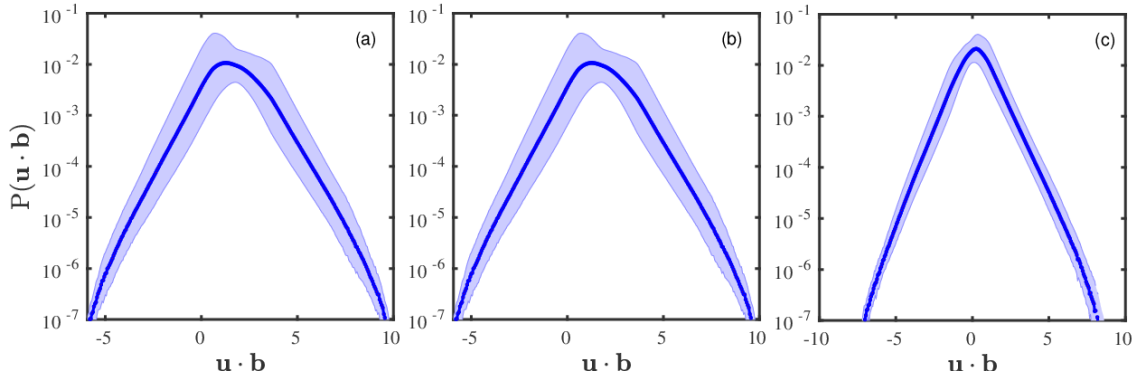


**Figure 10.** Semilog (base 10) plots of PDFs of the moduli of the cross helicity  $H_C = \mathbf{u} \cdot \mathbf{b}$  for (a)  $\text{Pr}_M = 0.1$ , (b)  $\text{Pr}_M = 1$ , and (c)  $\text{Pr}_M = 10$ , with the arguments of the PDFs scaled by their root-mean-square values. One-standard-deviation error bars are indicated by the shaded regions (cf. Figs. 18 (b.3), (c.3), and (d.3), for 3DMHD, in Ref. [32]).

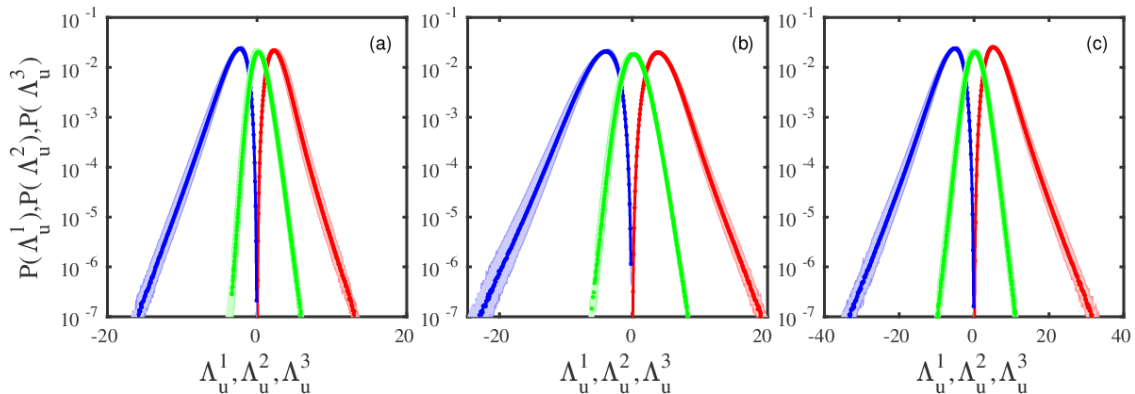


**Figure 11.** Semilog (base 10) plots of PDFs of eigenvalues  $\Lambda_u^1$  (red lines),  $\Lambda_u^2$  (green lines), and  $\Lambda_u^3$  (blue lines) of the rate-of-strain tensor  $\mathbb{S}$ ; for (a)  $\text{Pr}_M = 0.1$ , (b)  $\text{Pr}_M = 1$ , and (c)  $\text{Pr}_M = 10$ . Arguments of PDFs are scaled by their root-mean-square values. One-standard-deviation error bars are indicated by the shaded regions (Fig. 19 in Ref. [32] gives these PDFs for 3DMHD, but only for the case of decaying 3D MHD turbulence).

are given in Table 1. The result  $\mu_{H_C} \simeq 0$  indicates a strong tendency for the alignment or antialignment of  $\mathbf{u}$  and  $\mathbf{b}$  in 3DRFMHD, a property it shares with 3DMHD (cf. bottom row of Figs. 18 (b.3), (c.3), and (d.3), for 3DMHD, in Ref. [32]); of course, this alignment or antialignment is not perfect as can be seen from the broad PDF of  $H_C$ .

The PDFs of the eigenvalues  $\Lambda_u^1$  (red lines),  $\Lambda_u^2$  (green lines), and  $\Lambda_u^3$  (blue lines) of the rate-of-strain tensor  $\mathbb{S}$  are shown in figures 11 (a), (b), and (c) for  $\text{Pr}_M = 0.1$ ,  $\text{Pr}_M = 1$ , and  $\text{Pr}_M = 10$ . [We label the eigenvalues such that  $\Lambda_u^1 > \Lambda_u^2 > \Lambda_u^3$ .] These PDFs for 3DRFMHD are qualitatively similar to their fluid-turbulence or 3DMHD [32, 33] analogues. (Figure 19 in Ref. [32] gives these PDFs for 3DMHD, but only for the case of decaying 3D MHD turbulence, so a direct comparison is not possible.) We recall that

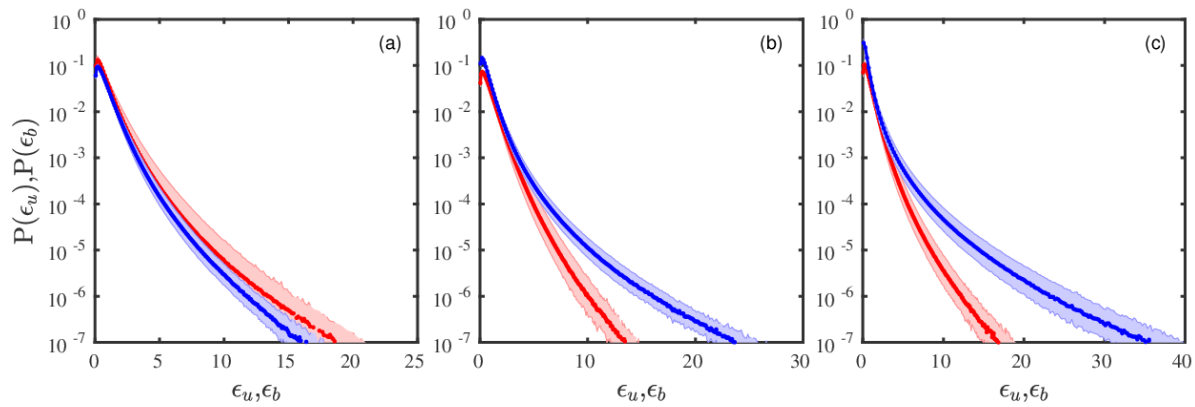


**Figure 12.** Semilog (base 10) plots of PDFs of the local kinetic-energy dissipation rate  $\epsilon_u$  (red lines) and the magnetic-energy dissipation rate  $\epsilon_b$  (blue lines), with the arguments scaled by their root-mean-square values for (a)  $\text{Pr}_M = 0.1$ , (b)  $\text{Pr}_M = 1$ , and (c)  $\text{Pr}_M = 10$ . One-standard-deviation error bars are indicated by the shaded regions (cf. Figs. 20 (b.3), (c.3), and (d.3), for 3DMHD, in Ref. [32]).

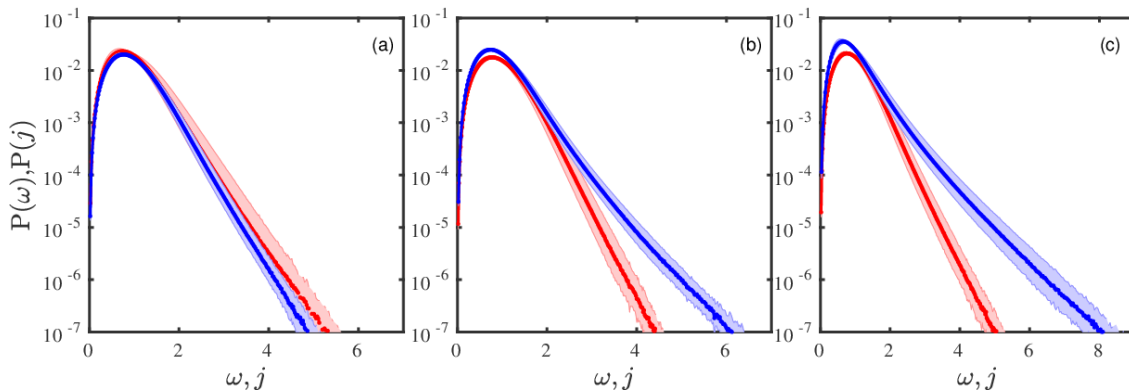


**Figure 13.** Semilog (base 10) plots of PDFs of the moduli of the local vorticity (red lines) and the current density (blue lines),  $\omega$  and  $j$ , respectively, with the arguments of the PDFs scaled by their root-mean-square values for (a)  $\text{Pr}_M = 0.1$ , (b)  $\text{Pr}_M = 1$ , and (c)  $\text{Pr}_M = 10$ . One-standard-deviation error bars are indicated by the shaded regions (cf. Figs. 21 (b.3), (c.3), and (d.3), for 3DMHD, in Ref. [32]).

these eigenvalues provide measures of the local stretching and compression of the fluid.

In figures 12 (a), (b), and (c) we show PDFs of the kinetic-energy dissipation rate  $\epsilon_u$  (red lines) and the magnetic-energy dissipation rate  $\epsilon_b$  (blue lines) for  $\text{Pr}_M = 0.1$ ,  $\text{Pr}_M = 1$ , and  $\text{Pr}_M = 10$ . All these PDFs have long tails; the tail of the PDF for  $\epsilon_b$  extends further than its counterpart for  $\epsilon_u$  as the magnetic Prandtl number is increased; these PDFs are similar to their counterparts for 3DMHD [32, 33] (cf. Figs. 20 (b.3), (c.3), and (d.3), for 3DMHD, in Ref. [32]). The tails of these PDFs indicates that large values of  $\epsilon_b$  are more likely to appear than large values of  $\epsilon_u$  and, given the long tails of these PDFs, suggests that, except at the smallest values of  $\text{Pr}_M$  we have used, we might obtain more marked intermittency for the magnetic field than for the velocity

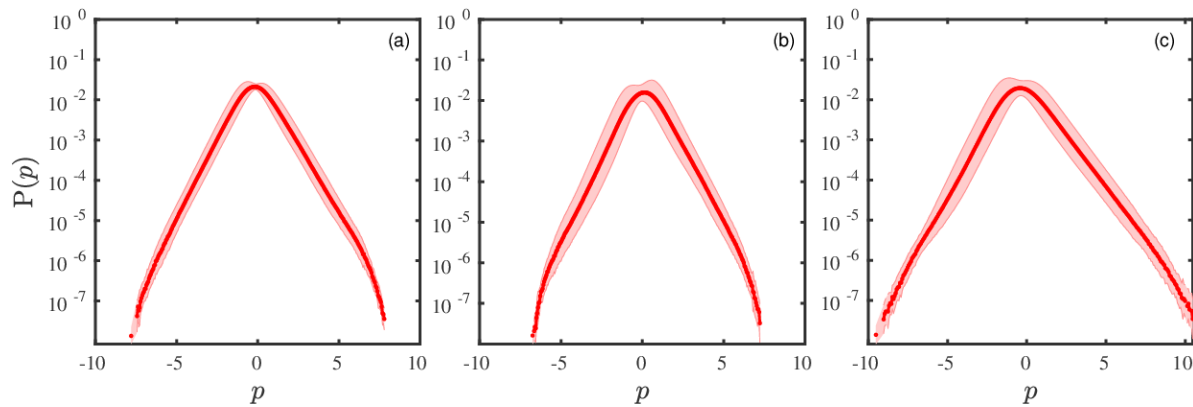


**Figure 14.** Semilog (base 10) plots of PDFs of local effective pressure fluctuations (red lines), with the arguments of the PDFs scaled by their root-mean-square values, for (a)  $\text{Pr}_M = 0.1$ , (b)  $\text{Pr}_M = 1$ , and (c)  $\text{Pr}_M = 10$ . One-standard-deviation error bars are indicated by the shaded regions (cf. Figs. 22 (b.2), (c.2), and (d.2), for 3DMHD, in Ref. [32]).

field. The means  $\mu_{\epsilon_u}$  and  $\mu_{\epsilon_b}$ , standard deviations  $\sigma_{\epsilon_u}$  and  $\sigma_{\epsilon_b}$ , skewnesses  $\gamma_{3,\epsilon_u}$  and  $\gamma_{3,\epsilon_b}$ , and kurtoses  $\gamma_{4,\epsilon_u}$  and  $\gamma_{4,\epsilon_b}$  of the local dissipation rates are given in Table 3.

Similar trends emerge if we examine the PDFs of the moduli of the vorticity and the current density  $\omega$  (red lines) and  $j$  (blue lines), respectively. These are shown in figures 13 (a), (b), and (c) for  $\text{Pr}_M = 0.1$ ,  $\text{Pr}_M = 1$ , and (c)  $\text{Pr}_M = 10$ . The tail of the PDF for  $j$  extends further than the tail of that for  $\omega$  as we increase the Prandtl number, which again indicates more intermittency for the magnetic field than for the velocity field with increasing  $\text{Pr}_M$ . These PDFs are also similar to their counterparts for 3DMHD [32, 33] (cf. Figs. 21 (b.3), (c.3), and (d.3), for 3DMHD, in Ref. [32]). The means  $\mu_\omega$  and  $\mu_j$ , standard deviations  $\sigma_\omega$  and  $\sigma_j$ , skewnesses  $\gamma_{3,\omega}$  and  $\gamma_{3,j}$ , and kurtoses  $\gamma_{4,\omega}$  and  $\gamma_{4,j}$  of the moduli of local vorticity and current density are given in Table 2.

Probability distribution functions of the local effective pressure (red lines) are shown in figures 14 (a), (b), and (c) for  $\text{Pr}_M = 0.1$ ,  $\text{Pr}_M = 1$ , and  $\text{Pr}_M = 10$ , respectively. As in 3DMHD (cf. Figs. 22 (b.2), (c.2), and (d.2) in Ref. [32]), these PDFs for 3DRFMHD are (a) distinctly non-Gaussian, (b) peaked at the  $\mu_p = 0$ , and (c) are positively skewed, for  $\text{Pr}_M = 1$ ,  $\text{Pr}_M = 10$ , and  $\text{Pr}_M = 0.1$ . The mean  $\mu_p$ , standard deviation  $\sigma_p$ , skewness  $\gamma_{3,p}$ , and kurtosis  $\gamma_{4,p}$  of the effective pressure are given in Table 4.

*3.3.1. PDFs of velocity- and magnetic-field gradients* To examine closely the nature of intermittency in 3DRFMHD we study the length-scale dependence of PDFs of increments of velocity and magnetic fields of the form  $\delta a_{\parallel}(\mathbf{x}, l) \equiv \mathbf{a}(\mathbf{x} + \mathbf{l}, t) - \mathbf{a}(\mathbf{x}, t) \cdot \frac{\mathbf{l}}{l}$ , with  $\mathbf{a}$  either  $\mathbf{u}$  or  $\mathbf{b}$ ,  $l = |\mathbf{l}|$  the length scale, and  $\mathbf{x}$  an origin over which we can average to determine the dependence of the PDFs of  $\delta a_{\parallel}$  on the scale  $l$ ; for notational convenience, such velocity and magnetic-field increments are denoted by  $\delta u(l)$  and  $\delta b(l)$  in our plots.

Figures 15 (a), (b), and (c) show these PDFs for  $\text{Pr}_M = 0.1$ ,  $\text{Pr}_M = 1$ , and  $\text{Pr}_M = 10$ , respectively. The PDFs of velocity increments are shown for separations  $l = 2\delta x$  (red

**Table 1.** The mean  $\mu_{H_C}$ , standard deviation  $\sigma_{H_C}$ , skewness  $\mu_{3,H_C}$ , and kurtosis  $\mu_{4,H_C}$  of the PDF of the cross helicity  $H_C$  for our runs for 3DRFMHD; columns 6 and 7 give, respectively, the mean energy  $E$  and ratio of the means of the cross helicity and the energy, i.e.,  $\mu_{H_C}/E$ .

$\text{Pr}_M$	$\mu_{H_C}$	$\sigma_{H_C}$	$\gamma_{3,H_C}$	$\gamma_{4,H_C}$	$E$	$\mu_{H_C}/E$
0.1	0.04	0.03	0.30	3.00	0.07	0.58
1	0.16	0.14	0.30	3.00	0.31	0.52
10	0.02	0.12	0.02	4.13	0.35	0.06

**Table 2.** The mean  $\mu$ , standard deviation  $\sigma$ , skewness  $\gamma_3$ , and kurtosis  $\gamma_4$  of the PDFs of the modulus of the local vorticity  $\omega$  and local current density  $j$ .

$\text{Pr}_M$	$\mu_\omega$	$\sigma_\omega$	$\gamma_{3,\omega}$	$\gamma_{4,\omega}$	$\mu_j$	$\sigma_j$	$\gamma_{3,j}$	$\gamma_{4,j}$
0.1	2.66	1.30	1.01	4.90	2.08	0.96	0.89	4.49
1	4.61	2.09	0.78	3.99	5.06	2.45	1.16	5.97
10	5.52	2.59	0.92	4.59	8.28	4.69	1.79	9.64

**Table 3.** The mean  $\mu$ , standard deviation  $\sigma$ , skewness  $\gamma_3$ , and kurtosis  $\gamma_4$  of the PDFs of the modulus of the local energy dissipation rates  $\epsilon_u$  and  $\epsilon_b$ .

$\text{Pr}_M$	$\mu_{\epsilon_u}$	$\sigma_{\epsilon_u}$	$\gamma_{3,\epsilon_u}$	$\gamma_{4,\epsilon_u}$	$\mu_{\epsilon_b}$	$\sigma_{\epsilon_b}$	$\gamma_{3,\epsilon_b}$	$\gamma_{4,\epsilon_b}$
0.1	$1.7 \times 10^{-3}$	$1.7 \times 10^{-3}$	3.21	24.85	$1.0 \times 10^{-2}$	$1.0 \times 10^{-2}$	2.86	20.16
1	$5.0 \times 10^{-2}$	$4.7 \times 10^{-2}$	2.45	14.48	$6.1 \times 10^{-2}$	$6.6 \times 10^{-2}$	4.17	45.06
10	$7.2 \times 10^{-2}$	$7.1 \times 10^{-2}$	2.96	21.50	$1.7 \times 10^{-2}$	$2.5 \times 10^{-2}$	6.84	110.8

**Table 4.** The mean  $\mu_p$ , standard deviation  $\sigma_p$ , skewness  $\gamma_{3,p}$ , and kurtosis  $\gamma_{4,p}$  of the PDFs of the local effective pressure  $\bar{p}$ .

$\text{Pr}_M$	$\mu_p$	$\sigma_p$	$\gamma_{3,p}$	$\gamma_{4,p}$
0.1	$-7 \times 10^{-3}$	0.05	0.19	4.12
1	$4 \times 10^{-3}$	0.05	0.03	3.49
10	$-2 \times 10^{-2}$	0.08	0.34	3.85

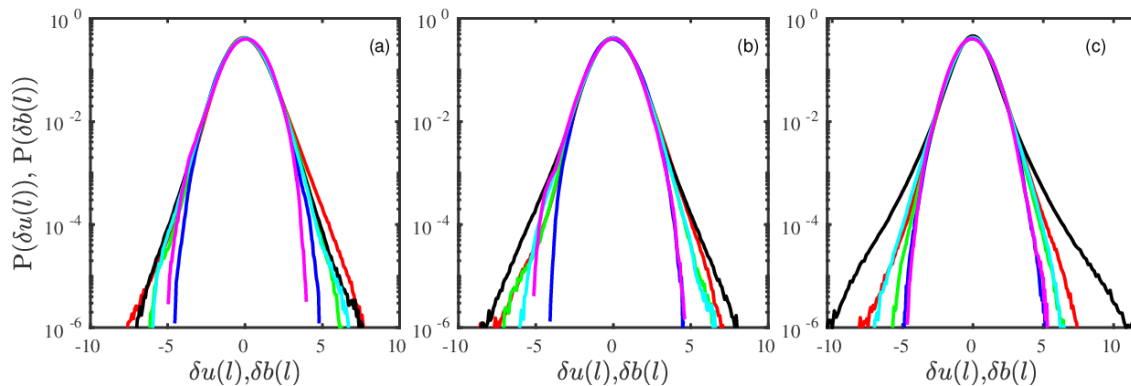


**Figure 15.** Semilog (base 10) plots of PDFs of velocity increments  $\delta u(l)$ , for separations  $l = 2\delta x$  (red lines),  $10\delta x$  (green lines), and  $100\delta x$  (blue lines), and of magnetic-field increments  $\delta b(l)$ , for separations  $l = 2\delta x$  (black lines),  $10\delta x$  (cyan lines), and  $100\delta x$  (magenta lines) for (a)  $\text{Pr}_M = 0.1$ , (b)  $\text{Pr}_M = 1$ , and (c)  $\text{Pr}_M = 10$  (cf. Figs. 23 (b.3), (c.3), and (d.3), for 3DMHD, in Ref. [32]). Arguments of these PDFs are scaled by their root-mean-square values.

lines),  $l = 10\delta x$  (green lines), and  $l = 100\delta x$  (blue lines), where  $\delta x$  is our real-space lattice spacing; for PDFs of magnetic-field increments we also use the separations  $l = 2\delta x$  (black lines),  $l = 10\delta x$  (cyan lines), and  $l = 100\delta x$  (magenta lines). As in 3DMHD (cf. Figs. 23 (b.3), (c.3), and (d.3) in Ref. [32]), we see that these PDFs are nearly Gaussian if the length scale  $l$  is large. As  $l$  decreases, the PDFs develop long, non-Gaussian tails, a clear signature of intermittency. Furthermore, a comparison of the red and black lines in these plots indicates that the PDFs of the magnetic-field increments are broader than their velocity counterparts for  $\text{Pr}_M = 1$  and  $\text{Pr}_M = 10$  and the trend reverses for  $\text{Pr}_M = 0.1$ . This is again because of the stronger intermittency in the magnetic-field than that in velocity field at large  $\text{Pr}_M$ , a result we have also found for 3DMHD [32, 33] from DNS studies with higher than those presented for 3DRFMHD here.

The general trend that we notice from these PDFs is that the magnetic field is more intermittent than the velocity field at large Prandtl numbers but this difference decreases as  $\text{Pr}_M$  is lowered. We quantify this below by obtaining multiscaling exponents of velocity and magnetic-field structure functions in subsection 3.4.

**3.3.2. PDFs of angles** The angles between various vectors, in 3DRFMHD turbulence, give us some understanding of the nature of flows. Here we present PDFs of cosines of angles between various vectors and the three eigenvectors of  $\mathbb{S}$  that give directions of stretching and compression.

In figures 16 (a), (b), and (c) we show, for  $\text{Pr}_M = 0.1$ ,  $\text{Pr}_M = 1$ , and  $\text{Pr}_M = 10$ , respectively, the PDFs of cosines of angles between the vorticity  $\boldsymbol{\omega}$  and the eigenvectors of the fluid rate-of-strain tensor  $\mathbb{S}$ , namely  $\hat{e}_u^1$  [red line],  $\hat{e}_u^2$  [blue line], and  $\hat{e}_u^3$  [green line]. As in 3DMHD (cf. Figs. 13 for *decaying* 3DMHD turbulence in Ref. [32]), we find that  $\boldsymbol{\omega}$  is preferentially aligned or anti-aligned with  $\hat{e}_u^2$  for all  $\text{Pr}_M$  in 3DRFMHD. There



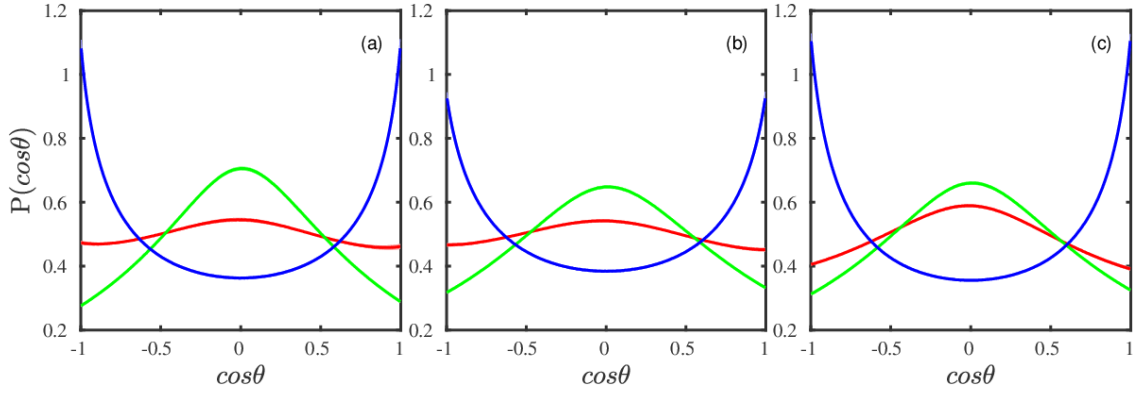


**Figure 16.** Plots of the PDFs of cosines of angles between the vorticity  $\boldsymbol{\omega}$  and the eigenvectors of the fluid rate-of-strain tensor  $\mathbb{S}$ , namely  $\hat{e}_u^1$  [red line],  $\hat{e}_u^2$  [blue line], and  $\hat{e}_u^3$  [green line]; for (a)  $\text{Pr}_M = 0.1$ , (b)  $\text{Pr}_M = 1$ , and (c)  $\text{Pr}_M = 10$  (cf. Figs. 13 for *decaying* 3DMHD turbulence in Ref. [32]). One-standard-deviation error bars are indicated by the shaded regions.

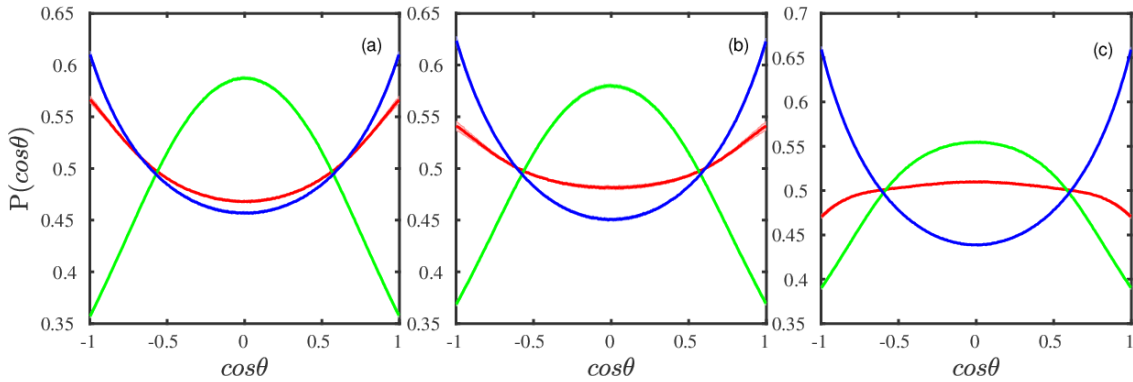


**Figure 17.** Plots of the PDFs of cosines of angles between the current density  $\mathbf{j}$  and the eigenvectors of the fluid rate-of-strain tensor  $\mathbb{S}$ , namely  $\hat{e}_u^1$  [red line],  $\hat{e}_u^2$  [blue line], and  $\hat{e}_u^3$  [green line]; for (a)  $\text{Pr}_M = 0.1$ , (b)  $\text{Pr}_M = 1$ , and (c)  $\text{Pr}_M = 10$  (cf. Fig. 14 for *decaying* 3DMHD turbulence in Ref. [32]). One-standard-deviation error bars are indicated by the shaded regions.

is some tendency for perpendicular alignment of  $\boldsymbol{\omega}$  with  $\hat{e}_u^1$  and  $\hat{e}_u^3$  for all  $\text{Pr}_M$  and no preferential angle with  $\hat{e}_u^2$ .

In figures 17 (a), (b), and (c) we show, for  $\text{Pr}_M = 0.1$ ,  $\text{Pr}_M = 1$ , and  $\text{Pr}_M = 10$ , respectively, the PDFs of cosines of angles between the current density  $\mathbf{j}$  and the eigenvectors of the fluid rate-of-strain tensor  $\mathbb{S}$ , namely  $\hat{e}_u^1$  [red line],  $\hat{e}_u^2$  [blue line], and  $\hat{e}_u^3$  [green line]. The alignment or anti-alignment tendencies in this case are not as strong as for  $\boldsymbol{\omega}$ . We see that  $\mathbf{j}$  has some tendency to be perpendicular to  $\hat{e}_u^3$  and shows preferential alignment or anti-alignment along  $\hat{e}_u^1$  and  $\hat{e}_u^2$  for all values of  $\text{Pr}_M$  we have studied. These PDFs for 3DRFMHD are slightly different from their counterparts in 3DMHD [32, 33]; but we note that Fig. 14 in Ref. [32] has data only for *decaying* 3DMHD turbulence.

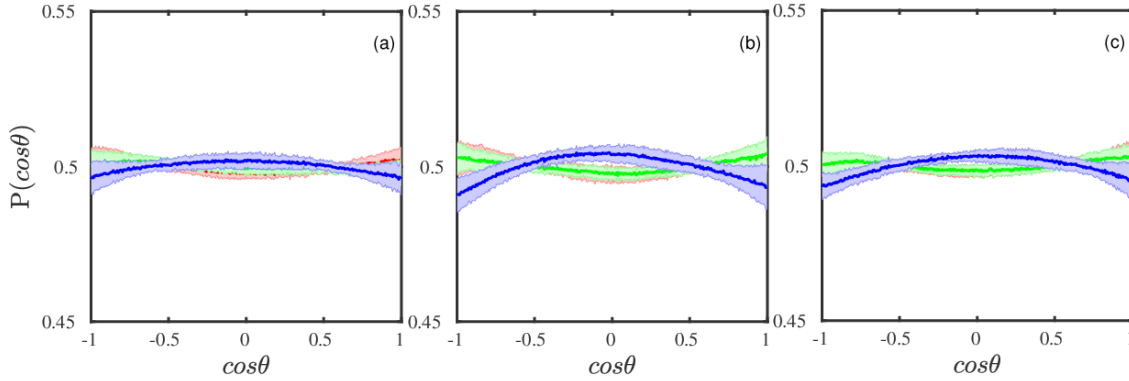


**Figure 18.** Semilog (base 10) plots of the PDFs of cosines of angles between the velocity  $\mathbf{u}$  and the eigenvectors of the fluid rate-of-strain tensor  $\mathbb{S}$ , namely  $\hat{e}_u^1$  [red line],  $\hat{e}_u^2$  [blue line], and  $\hat{e}_u^3$  [green line]; for (a)  $\text{Pr}_M = 0.1$ , (b)  $\text{Pr}_M = 1$ , and (c)  $\text{Pr}_M = 10$  (cf. Fig. 15 for *decaying* 3DMHD turbulence in Ref. [32]). One-standard-deviation error bars are indicated by the shaded regions.

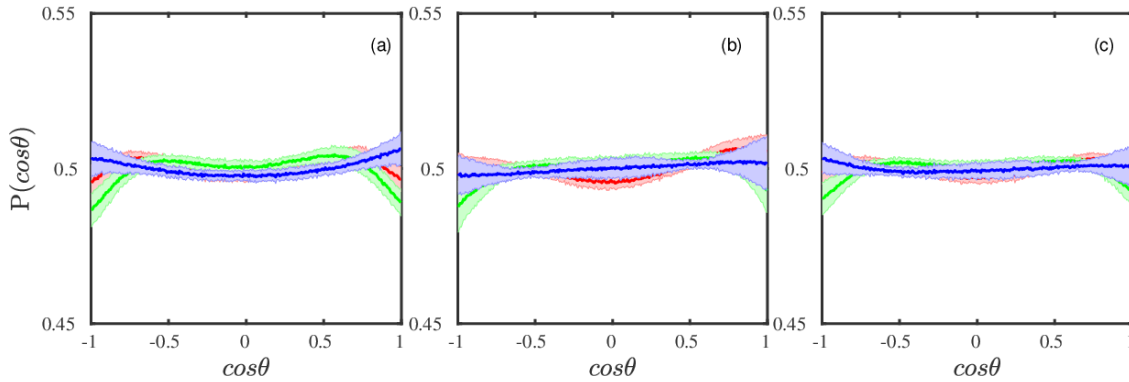


**Figure 19.** Plots of the PDFs of cosines of angles between the magnetic field  $\mathbf{b}$  and the eigenvectors of the fluid rate-of-strain tensor  $\mathbb{S}$ , namely  $\hat{e}_u^1$  [red line],  $\hat{e}_u^2$  [blue line], and  $\hat{e}_u^3$  [green line]; for (a)  $\text{Pr}_M = 0.1$ , (b)  $\text{Pr}_M = 1$ , and (c)  $\text{Pr}_M = 10$  (cf. Fig. 16 for *decaying* 3DMHD turbulence in Ref. [32]). One-standard-deviation error bars are indicated by the shaded regions.

In figures 18 (a), (b), and (c), we show for  $\text{Pr}_M = 0.1$ ,  $\text{Pr}_M = 1$ , and  $\text{Pr}_M = 10$ , respectively, PDFs of the cosines of the angles between the velocity field  $\mathbf{u}$  and the eigenvectors of the fluid rate-of-strain tensor  $\mathbb{S}$ , namely  $\hat{e}_u^1$  [red line],  $\hat{e}_u^2$  [blue line], and  $\hat{e}_u^3$  [green line]. These PDFs indicate that there is no preferred angle between the velocity field and the eigenvectors of  $\mathbb{S}$  for all the values of  $\text{Pr}_M$  we have studied. This behavior of 3DRFMHD is completely different from that found for *decaying* 3DMHD [32, 33] turbulence, where the velocity  $\mathbf{u}$  tends to align or anti-align with  $\hat{e}_u^2$  and there is a weak tendency for an angle close to  $45^\circ$  (or  $135^\circ$ ) between  $\mathbf{u}$  and  $\hat{e}_u^1$  and  $\hat{e}_u^3$ . We note that Fig. 15 in Ref. [32] has data only for *decaying* 3DMHD turbulence.

Figures 19 (a), (b), and (c) show, for  $\text{Pr}_M = 0.1$ ,  $\text{Pr}_M = 1$ , and  $\text{Pr}_M = 10$ , respectively, the PDFs of the cosines of angles between the magnetic field  $\mathbf{b}$  and the

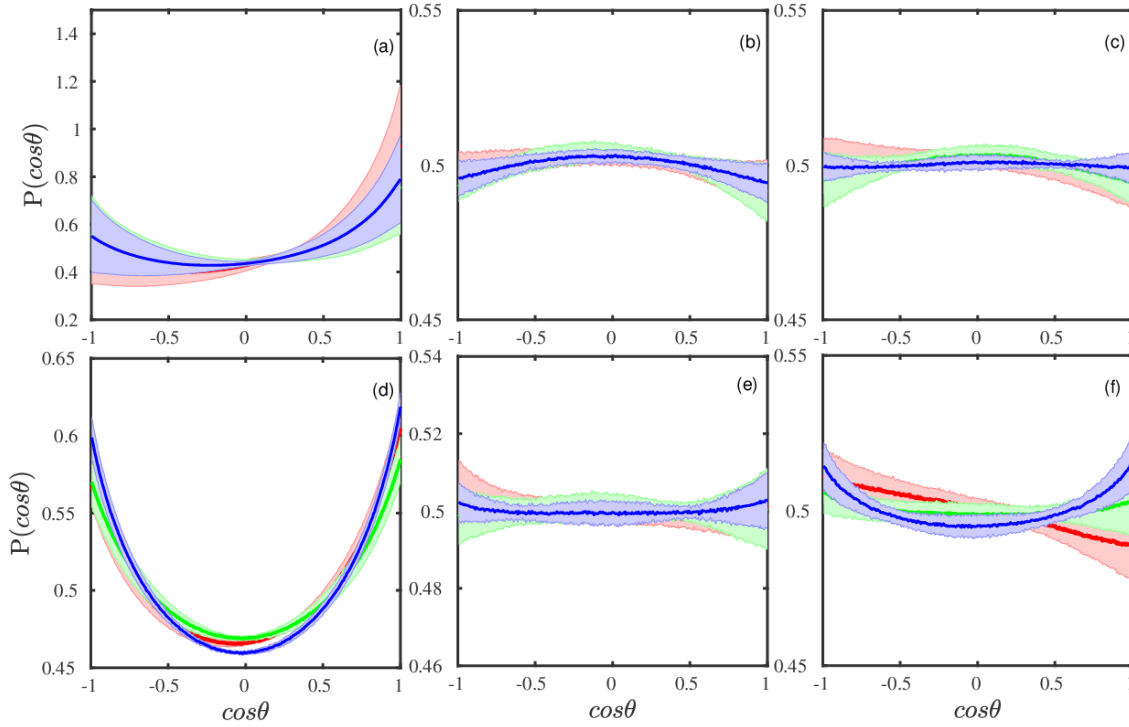


**Figure 20.** Plots of PDFs of cosines of angles between (a)  $\mathbf{u}$  and  $\mathbf{b}$ , (b)  $\mathbf{u}$  and  $\boldsymbol{\omega}$ , (c)  $\mathbf{u}$  and  $\mathbf{j}$ , (d)  $\boldsymbol{\omega}$  and  $\mathbf{j}$ , (e)  $\mathbf{b}$  and  $\boldsymbol{\omega}$ , and (f)  $\mathbf{b}$  and  $\mathbf{j}$  for  $\text{Pr}_M = 0.1$  (green line),  $\text{Pr}_M = 1$  (red line),  $\text{Pr}_M = 10$  (blue line) (cf. Fig. 17 for *decaying* 3DMHD turbulence in Ref. [32]). One-standard-deviation error bars are indicated by the shaded regions.

eigenvectors of the fluid rate-of-strain tensor  $\mathbb{S}$ , namely  $\hat{e}_u^1$  [red line],  $\hat{e}_u^2$  [blue line], and  $\hat{e}_u^3$  [green line]. At least at the level of resolution of our calculation, these PDFs do not show any clear trends with  $\text{Pr}_M$ . We note that Fig. 16 in Ref. [32] has data only for *decaying* 3DMHD turbulence.

Figures 20 (a), (b), (c), (d), (e), and (f) show, respectively, PDFs of the cosines of angles between  $\mathbf{u}$  and  $\mathbf{b}$ ,  $\mathbf{u}$  and  $\boldsymbol{\omega}$ ,  $\mathbf{u}$  and  $\mathbf{j}$ ,  $\boldsymbol{\omega}$  and  $\mathbf{j}$ ,  $\mathbf{b}$  and  $\boldsymbol{\omega}$ , and  $\mathbf{b}$  and  $\mathbf{j}$  for  $\text{Pr}_M = 0.1$  (green line),  $\text{Pr}_M = 1$  (red line), and  $\text{Pr}_M = 10$  (blue line). Figure 20 (a) shows that  $\mathbf{u}$  and  $\mathbf{b}$  are preferentially aligned for  $\text{Pr}_M = 1$  and  $\text{Pr}_M = 10$ . The alignment or anti-alignment, i.e., the probability of occurrence of *Beltrami correlations* ( $\cos\theta = \pm 1$ ) [77] implies the depletion of nonlinearity. From figures 20 (b) and (c) we see that there is no preferred angle between  $\mathbf{u}$  and  $\boldsymbol{\omega}$  and between  $\mathbf{u}$  and  $\mathbf{j}$ ; and there is very little Prandtl-number dependence in the PDFs shown in these figures. In Fig. 20 (d), we see  $\boldsymbol{\omega}$  and  $\mathbf{j}$  are preferentially aligned or anti-aligned for all  $\text{Pr}_M$ . From Figure 20 (e), we see there is no particularly preferred angle between  $\mathbf{b}$  and  $\boldsymbol{\omega}$  for  $\text{Pr}_M = 0.1$ ,  $\text{Pr}_M = 1$  and  $\text{Pr}_M = 10$ . Figure 20 (f) shows preferential alignment or anti-alignment between  $\mathbf{b}$  and  $\mathbf{j}$ , with a marginally greater tendency for the former than the latter, for  $\text{Pr}_M = 1$ . Figure 17 in Ref. [32] has data only for *decaying* 3DMHD turbulence.

## 3.4. Structure functions

We continue our elucidation of intermittency in 3DRFMHD turbulence by studying the scale dependence of order- $p$  equal-time, longitudinal velocity structure functions  $S_p^u(l) \equiv \langle |\delta u_{\parallel}(\mathbf{x}, l)|^p \rangle$  and longitudinal magnetic-field structure functions  $S_p^b(l) \equiv \langle |\delta b_{\parallel}(\mathbf{x}, l)|^p \rangle$ , respectively, where  $\delta u_{\parallel}(\mathbf{x}, l) \equiv \mathbf{u}(\mathbf{x}+\mathbf{l}, t) - \mathbf{u}(\mathbf{x}, t) \cdot \frac{\mathbf{l}}{l}$  and  $\delta b_{\parallel}(\mathbf{x}, l) \equiv \mathbf{b}(\mathbf{x}+\mathbf{l}, t) - \mathbf{b}(\mathbf{x}, t) \cdot \frac{\mathbf{l}}{l}$ . From these structure functions we also obtain the hyperflatnesses  $F_6^u(l) = S_6^u(l)/[S_2^u(l)]^3$  and  $F_6^b(l) = S_6^b(l)/[S_2^b(l)]^3$ .

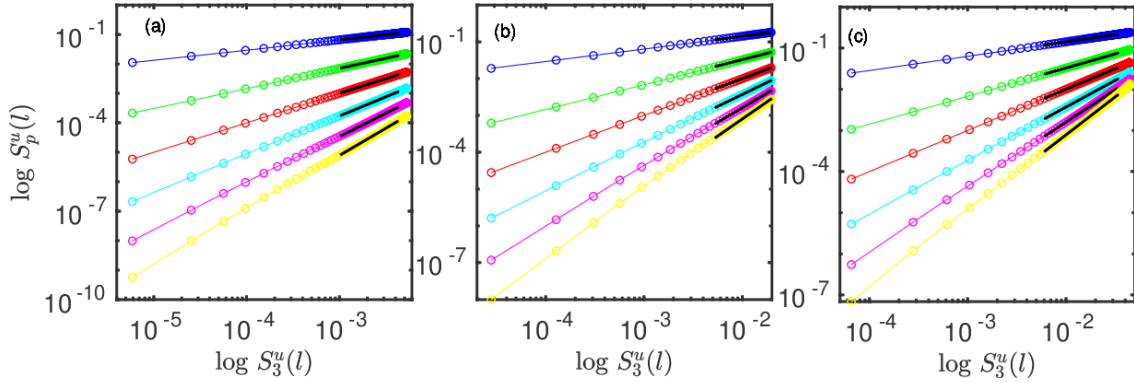


**Figure 21.** Log-log (base 10) extended-self-similarity (ESS) plots of velocity structure functions of order  $p$  versus that of order 3;  $p = 1$  (blue),  $p = 2$  (green),  $p = 3$  (red),  $p = 4$  (cyan),  $p = 5$  (magenta), and  $p = 6$  (yellow); for (a)  $\text{Pr}_M = 0.1$ , (b)  $\text{Pr}_M = 1$ , and (c)  $\text{Pr}_M = 10$ . The region marked with black line shows the range over which we calculate the exponent ratio  $\zeta_p^u/\zeta_3^u$  (cf. Figs. 25 (b.1), (c.1), and (d.1) in Ref. [32])

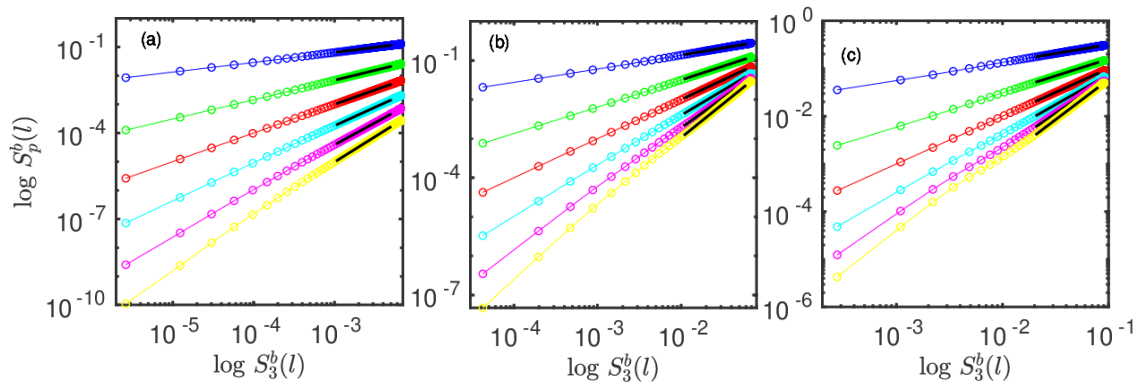


**Figure 22.** Log-log (base 10) ESS plots of magnetic-field structure functions of order  $p$  versus that of order 3;  $p = 1$  (blue),  $p = 2$  (green),  $p = 3$  (red),  $p = 4$  (cyan),  $p = 5$  (magenta), and  $p = 6$  (yellow); for (a)  $\text{Pr}_M = 0.1$ , (b)  $\text{Pr}_M = 1$ , and (c)  $\text{Pr}_M = 10$ . The region marked with a black line shows the range over which we calculate the exponent ratio  $\zeta_p^b/\zeta_3^b$  (cf. Figs. 25 (b.2), (c.2), and (d.2) in Ref. [32]).

For the inertial range  $\eta_d^u, \eta_d^b \ll l \ll L$ , we expect  $S_p^u(l) \sim l^{\zeta_p^u}$  and  $S_p^b(l) \sim l^{\zeta_p^b}$ , where  $\zeta_p^u$  and  $\zeta_p^b$  are inertial-range multiscaling exponents for velocity and magnetic

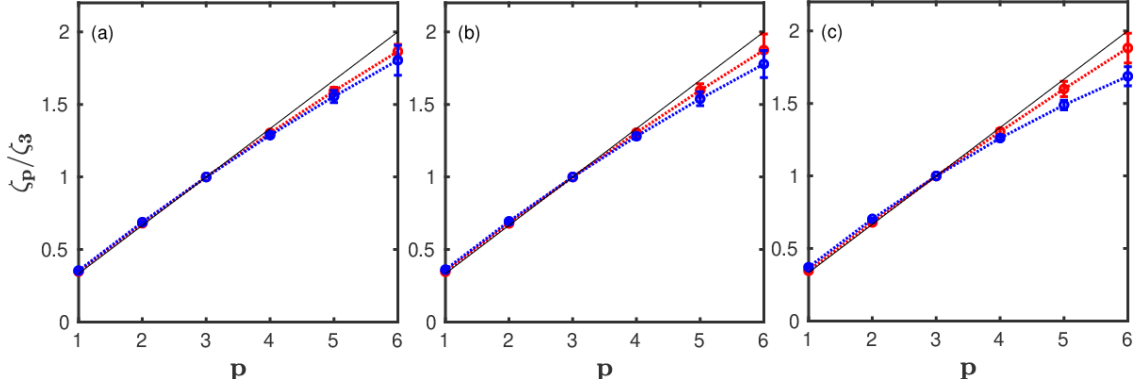


**Figure 23.** Multiscaling exponent ratios  $\zeta_p^u/\zeta_3^u$  (red line) and  $\zeta_p^b/\zeta_3^b$  (blue line) versus  $p$  for (a)  $\text{Pr}_M = 0.1$ , (b)  $\text{Pr}_M = 1$ , and (c)  $\text{Pr}_M = 10$  (cf. Figs. 25 (b.3), (c.3), and (d.3) in Ref. [32]).

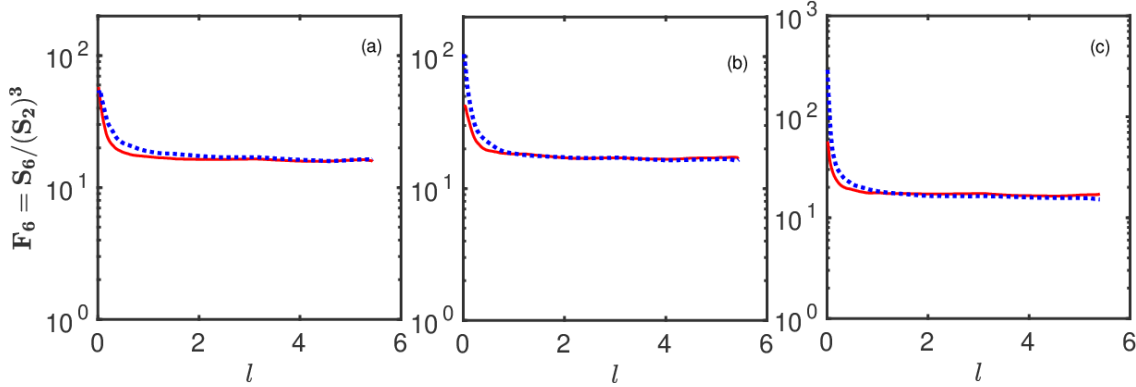


**Figure 24.** Semilog (base 10) plots of the hyperflatness of the velocity field  $F_6^u(l) = \frac{S_6^u(l)}{|S_3^u(l)|^3}$  (red line) and its magnetic counterpart  $F_6^b(l) = \frac{S_6^b(l)}{|S_3^b(l)|^3}$  (blue dashed line) for (a)  $\text{Pr}_M = 0.1$ , (b)  $\text{Pr}_M = 1$ , and (c)  $\text{Pr}_M = 10$  (cf. Figs. 25 (b.4), (c.4), and (d.4) in Ref. [32]).

**Table 5.** Multiscaling exponent ratios  $\zeta_p^u/\zeta_3^u$  and  $\zeta_p^b/\zeta_3^b$  from our DNS for 3DRFMHD turbulence.

$p$	$\zeta_p^u/\zeta_3^u; \zeta_p^b/\zeta_3^b(\text{Pr}_M = 0.1)$	$\zeta_p^u/\zeta_3^u; \zeta_p^b/\zeta_3^b(\text{Pr}_M = 1)$	$\zeta_p^u/\zeta_3^u; \zeta_p^b/\zeta_3^b(\text{Pr}_M = 10)$
1	$0.35 \pm 0.00; 0.35 \pm 0.00$	$0.35 \pm 0.00; 0.36 \pm 0.00$	$0.35 \pm 0.01; 0.37 \pm 0.00$
2	$0.68 \pm 0.00; 0.69 \pm 0.00$	$0.68 \pm 0.00; 0.69 \pm 0.00$	$0.68 \pm 0.01; 0.70 \pm 0.00$
3	$1.00 \pm 0.00; 1.00 \pm 0.00$	$1.00 \pm 0.00; 1.00 \pm 0.00$	$1.00 \pm 0.00; 1.00 \pm 0.00$
4	$1.30 \pm 0.01; 1.29 \pm 0.01$	$1.30 \pm 0.01; 1.28 \pm 0.01$	$1.30 \pm 0.02; 1.26 \pm 0.01$
5	$1.59 \pm 0.03; 1.56 \pm 0.04$	$1.60 \pm 0.05; 1.53 \pm 0.05$	$1.60 \pm 0.05; 1.49 \pm 0.03$
6	$1.86 \pm 0.05; 1.80 \pm 0.10$	$1.87 \pm 0.11; 1.78 \pm 0.10$	$1.88 \pm 0.10; 1.69 \pm 0.07$

fields, respectively; if these fields show multiscaling, we expect significant deviations from the K41 result  $\zeta_p^{uK41} = \zeta_p^{bK41} = p/3$ . [We do not have any mean magnetic field in our simulations, so we do not expect any Iroshnikov-Kraichnan [60] scaling.] Given large inertial ranges, the multiscaling exponents can be extracted from slopes of log-log plots of structure functions versus  $l$ . In DNSs, such as the ones presented here, inertial ranges are limited by the spatial resolution, so we use the extended-self-similarity (ESS) procedure [61, 62] in which we determine the multiscaling exponent ratios  $\zeta_p^u/\zeta_3^u$  and  $\zeta_p^b/\zeta_3^b$ , respectively, from slopes of log-log plots of  $S_p^u$  versus  $S_3^u$  and  $S_p^b$  versus  $S_3^b$ . The structure functions with ESS are shown in figures 21 and 22.

Figures 23 show the plots of exponent ratios  $\zeta_p^u/\zeta_3^u$  (red line with circles) and  $\zeta_p^b/\zeta_3^b$  (blue line with asterisks) versus order  $p$  for (a)  $\text{Pr}_M = 0.1$ , (b)  $\text{Pr}_M = 1$ , and (c)  $\text{Pr}_M = 10$ . The black solid line shows the K41 result for comparison. These plots show significant deviations from the K41 result, especially for  $p > 3$ , as in 3DMHD [32, 33], both for velocity and magnetic fields; this provides an effective measure of inertial-range intermittency. We observe from these plots that, at large values of  $\text{Pr}_M$ , the magnetic field is more intermittent than the velocity field as the deviations of  $\zeta_p^b/\zeta_3^b$  from the K41 result  $p/3$  are larger than those of  $\zeta_p^u/\zeta_3^u$ . This behavior in 3DRFMHD is similar to its counterpart in 3DMHD [32, 33] (cf. Figs. 25 (b.3), (c.3), and (d.3) in Ref. [32]).

Intermittency is also apparent in plots versus  $l$  of the hyperflatnesses  $F_6^u(l) = \frac{S_6^u(l)}{S_2^u(l)^3}$  (red line) and  $F_6^b(l) = \frac{S_6^b(l)}{S_2^b(l)^3}$  (blue dashed line) in Figs. 24 for (a)  $\text{Pr}_M = 0.1$ , (b)  $\text{Pr}_M = 1$ , and (c)  $\text{Pr}_M = 10$ . As  $l$  decreases,  $F_6^b(l)$  rises more rapidly than  $F_6^u(l)$  except for  $\text{Pr}_M = 0.1$ , in consonance with the trends mentioned in the previous paragraph.

### 3.5. Isosurfaces in RFMHD

Isosurfaces of moduli of the vorticity and current density,  $\omega$  and  $j$ , respectively, or energy dissipation rates and the effective pressure are useful ways of visualising structures in 3DMHD flows. In fluid turbulence isosurfaces of  $\omega$  show slender, tube-like structures if  $\omega$  is large; by contrast, in 3DMHD turbulence isosurfaces of  $\omega$  and  $j$  are organized into sheets [32, 33] (cf. Figs. 26 (b.3), (c.3), (d.3), and 27 (b.3), (c.3), (d.3) in Ref. [32]). Isosurfaces of the energy-dissipation-rates show sheets in both fluid and 3DMHD turbulence; and isosurfaces of the pressure in fluid turbulence, and of the effective pressure in 3DMHD turbulence are like clouds, with some tube-type structures in fluid turbulence.

In Figs. 25, 26, 27, 28, and 29 we show, respectively, isosurfaces of  $\omega$ ,  $j$ , the local kinetic-energy-dissipation rate  $\epsilon_u$ , the local magnetic-energy-dissipation rate  $\epsilon_b$ , and the local effective pressure  $\bar{p}$  for 3DRFMHD; the values of these quantities are chosen to be two standard deviations more than their mean values; the subplots in these figures show isosurface for (a)  $\text{Pr}_M = 0.1$ , (b)  $\text{Pr}_M = 1$ , and (c)  $\text{Pr}_M = 10$ . Even a cursory comparison of these isosurfaces with their analogues for 3DMHD [32, 33] shows that they are modified dramatically by the random, power-law forcing we employ here: in particular, isosurfaces of  $\omega$ ,  $j$ ,  $\epsilon_u$ ,  $\epsilon_b$ , and the effective pressure appear to be completely stippled

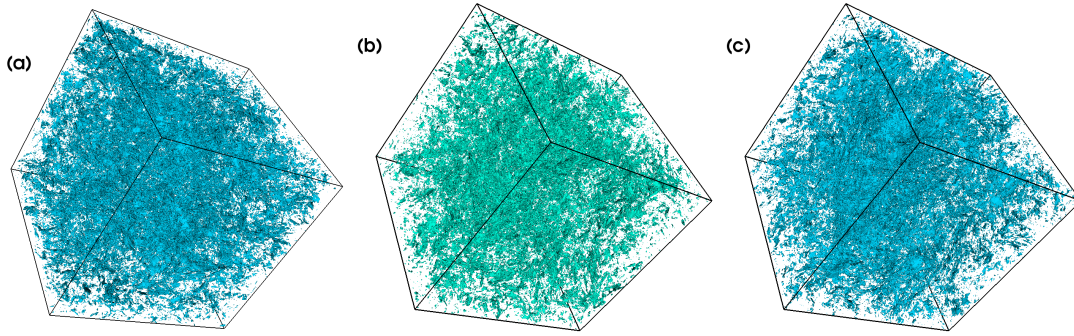


**Figure 25.** Isosurfaces of the modulus of the vorticity  $\omega$  in 3DRFMHD for (a)  $\text{Pr}_M = 0.1$ , (b)  $\text{Pr}_M = 1$ , and (c)  $\text{Pr}_M = 10$  and values of  $\omega$  that are two standard deviations more than its mean value (cf. Figs. 26 (b.3), (c.3), and (d.3) in Ref. [32]).

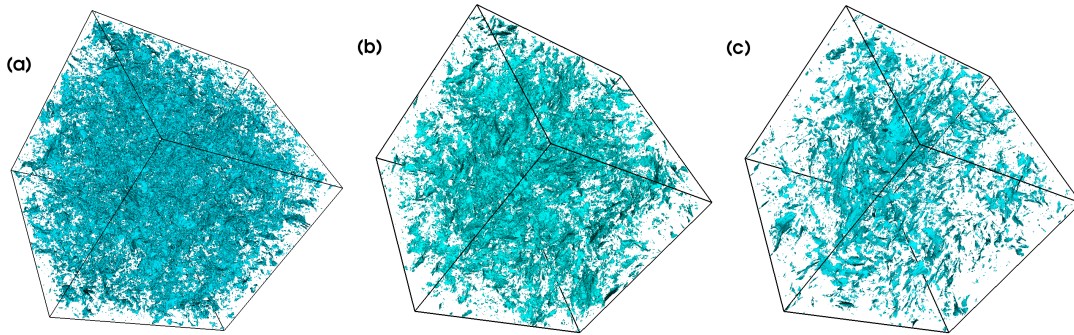


**Figure 26.** Isosurfaces of the modulus of the current density  $j$  in 3DRFMHD for (a)  $\text{Pr}_M = 0.1$ , (b)  $\text{Pr}_M = 1$ , and (c)  $\text{Pr}_M = 10$  and values of  $j$  that are two standard deviations more than its mean value (cf. Figs. 27 (b.3), (c.3), and (d.3) in Ref. [32]).

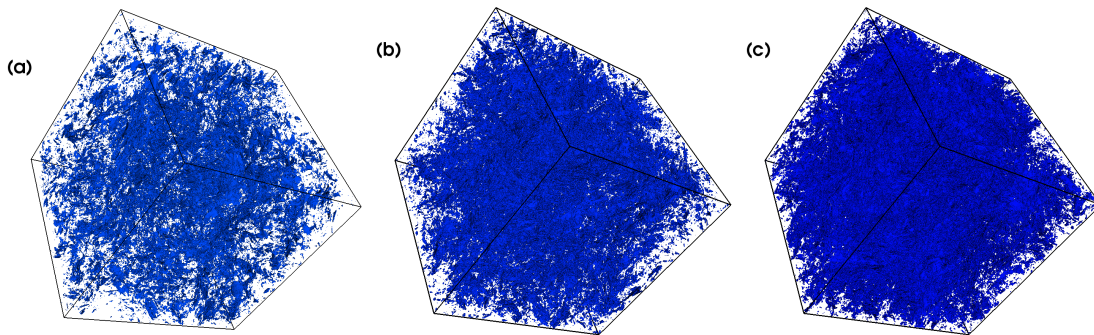


**Figure 27.** Isosurfaces of  $\epsilon_u$  in 3DRFMHD for (a)  $\text{Pr}_M = 0.1$ , (b)  $\text{Pr}_M = 1$ , and (c)  $\text{Pr}_M = 10$  and values of  $\epsilon_u$  that are two standard deviations more than its mean value (cf. Figs. 28 (b.3), (c.3), and (d.3) in Ref. [32]).

versions of the sheet-type isosurfaces that are seen in 3DMHD turbulence [32, 33]; this is reminiscent of the destruction of tube-type isosurfaces of  $\omega$  by power-law, random

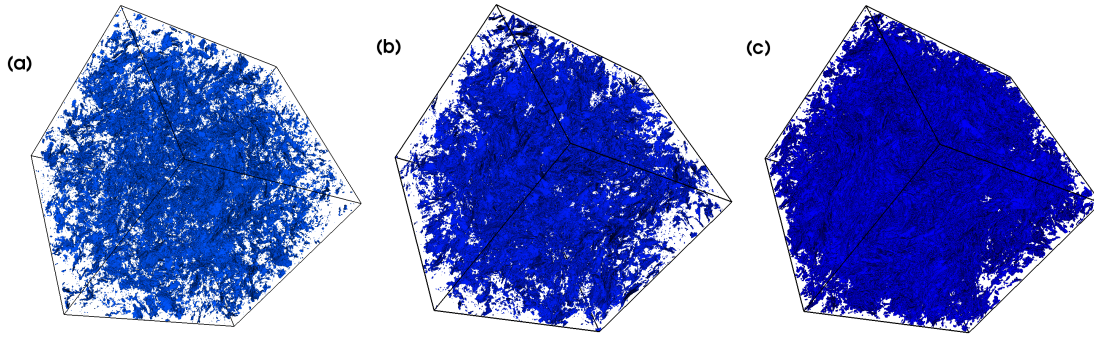


**Figure 28.** Isosurfaces of  $\epsilon_b$  in 3DRFMHD for (a)  $\text{Pr}_M = 0.1$ , (b)  $\text{Pr}_M = 1$ , and (c)  $\text{Pr}_M = 10$  and values of  $\epsilon_b$  that two standard deviations more than its mean value (cf. Figs. 29 (b.3), (c.3), and (d.3) in Ref. [32])

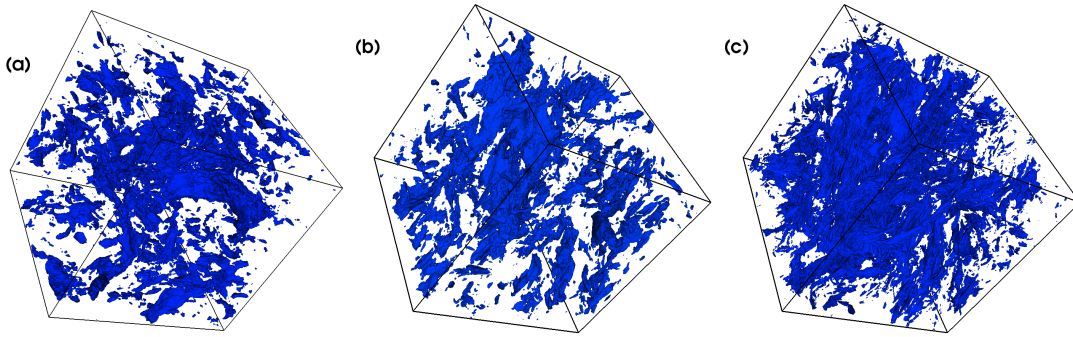


**Figure 29.** Isosurfaces of the effective pressure in 3DRFMHD for (a)  $\text{Pr}_M = 0.1$ , (b)  $\text{Pr}_M = 1$ , and (c)  $\text{Pr}_M = 10$  and values the effective pressure that are two standard deviations more than its mean value (cf. Figs. 30 (b.2), (c.2), and (d.2) in Ref. [32])

forcing in 3D Navier-Stokes turbulence [51].

### 3.6. Joint PDFs

In this subsection we present a set of joint PDFs for 3DRFMHD and we compare them with their analogues for 3DMHD [32, 33]. In particular, we give  $QR$  plots, and joint PDFs of  $\omega$  and  $j$ , of  $\epsilon_u$  and  $\epsilon_b$ , of  $\omega$  and  $\epsilon_u$ , and of  $j$  and  $\epsilon_b$ .

Figures 30 (a), (b), and (c) show  $QR$  plots, i.e., joint PDFs of  $Q$  and  $R$  for 3DRFMHD, via filled contour plots on a logarithmic scale, for  $\text{Pr}_M = 0.1$ ,  $\text{Pr}_M = 1$ , and  $\text{Pr}_M = 10$ , respectively. The black curve in these plots is the zero-discriminant line  $D \equiv \frac{27}{4}R^2 + Q^3 = 0$ . These  $QR$  plots retain, aside from some distortions, the characteristic tear-drop structure familiar from such plots fluid turbulence [2] and 3DMHD [32, 33]. Notice that, as we increase  $\text{Pr}_M$ , there is a decrease in the probability of having large values of  $Q$  and  $R$ , i.e., regions of large strain or vorticity are suppressed,



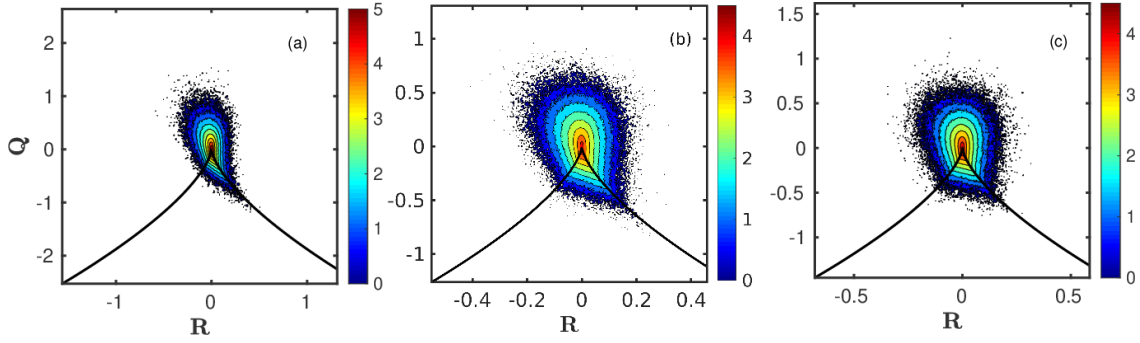


**Figure 30.**  $QR$  plots, i.e., joint PDFs of  $Q$  and  $R$ , in 3DRFMHD shown as filled contour plots on a logarithmic scale for (a)  $\text{Pr}_M = 0.1$ , (b)  $\text{Pr}_M = 1$ , and (c)  $\text{Pr}_M = 10$ . The arguments  $Q$  and  $R$  of the joint PDF are normalized by  $\langle \omega^2 \rangle$  and  $\langle \omega^2 \rangle^{3/2}$ , respectively. The black curve shows the zero-discriminant line  $D \equiv \frac{27}{4} R^2 + Q^3 = 0$  (cf. Figs. 31 (b.3), (c.3), and (d.3) in Ref. [32]).

as we have also found in 3DMHD (cf. Figs. 31 (b.2), (c.2), and (d.2) in Ref. [32]).

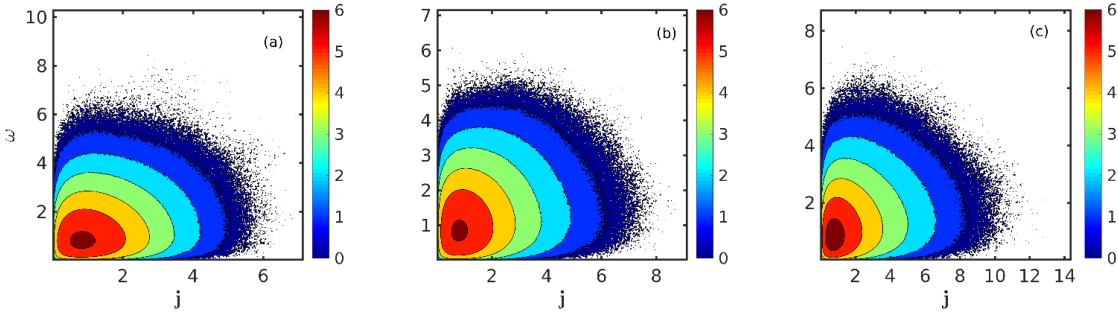


**Figure 31.** Joint PDFs of  $\omega$  and  $j$  for 3DRFMHD shown as filled contour plots on a logarithmic scale for (a)  $\text{Pr}_M = 0.1$ , (b)  $\text{Pr}_M = 1$ , and (c)  $\text{Pr}_M = 10$ . The arguments of the joint PDFs are normalized by their mean values (cf. Figs. 32 (b.3), (c.3), and (d.3) in Ref. [32]).

Joint PDFs of  $\omega$  and  $j$  for  $\text{Pr}_M = 0.1$ ,  $\text{Pr}_M = 1$ , and  $\text{Pr}_M = 10$  are shown in figures 31 (a), (b), and (c), respectively, for 3DRFMHD. These petal-shaped joint PDFs have long tails. As we move away from  $\text{Pr}_M = 1$  these joint PDFs are distorted such that large values of  $j$  are suppressed if  $\text{Re}_{M\lambda}$  is low, as in Fig. 31 (a), whereas large values of  $\omega$  are suppressed if  $\text{Re}_\lambda$  is low, as in figure 31 (c). These trends are similar to those in 3DMHD turbulence (cf. Figs. 32 (b.3), (c.3), and (d.3) in Ref. [32]).

Joint PDFs of  $\epsilon_u$  and  $\epsilon_b$  for  $\text{Pr}_M = 0.1$ ,  $\text{Pr}_M = 1$ , and  $\text{Pr}_M = 10$  are shown in figures 32 (a), (b), and (c). All these joint PDFs have long tails. As we move away from  $\text{Pr}_M = 1$  these joint PDFs change slightly such that large values of  $\epsilon_b$  are suppressed if  $\text{Re}_{M\lambda}$  is low, as in Fig. 32 (a), whereas large values of  $\epsilon_u$  are suppressed if  $\text{Re}_\lambda$  is low, as in Fig. 32 (c). These trends are similar to those in 3DMHD turbulence (cf. Figs. 33 (b.3), (c.3), and (d.3) in Ref. [32]).

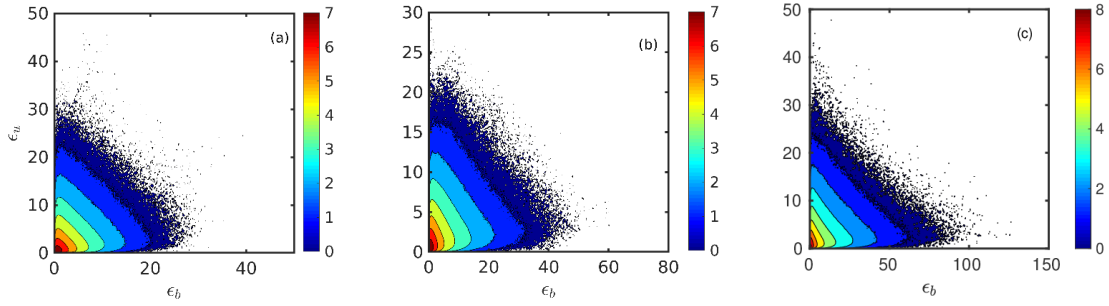


**Figure 32.** Joint PDFs of  $\epsilon_u$  and  $\epsilon_b$  for 3DRFMHD shown as filled contour plots on a logarithmic scale for (a)  $\text{Pr}_M = 0.1$ , (b)  $\text{Pr}_M = 1$ , and (c)  $\text{Pr}_M = 10$ . The arguments of the joint PDFs are normalized by their mean values (cf. Figs. 33 (b.3), (c.3), and (d.3) in Ref. [32]).

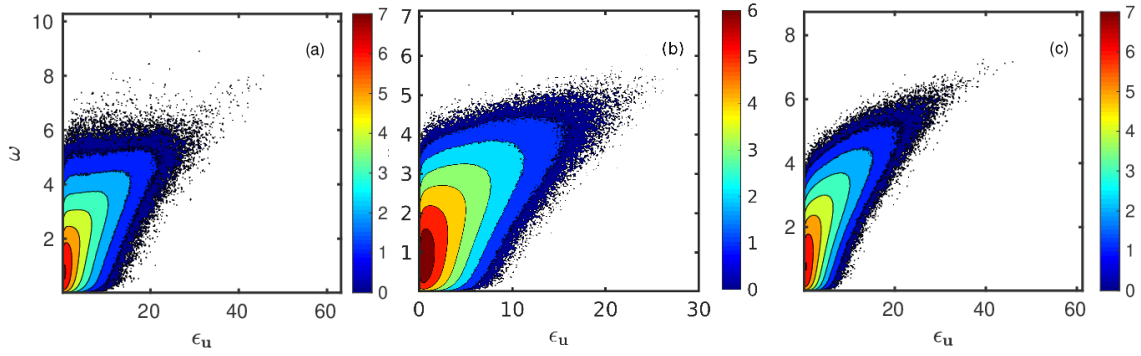


**Figure 33.** Joint PDFs of  $\omega$  and  $\epsilon_u$  for 3DRFMHD shown as filled contour plots on a logarithmic scale for (a)  $\text{Pr}_M = 0.1$ , (b)  $\text{Pr}_M = 1$ , and (c)  $\text{Pr}_M = 10$ . The arguments of the joint PDFs are normalized by their mean values.

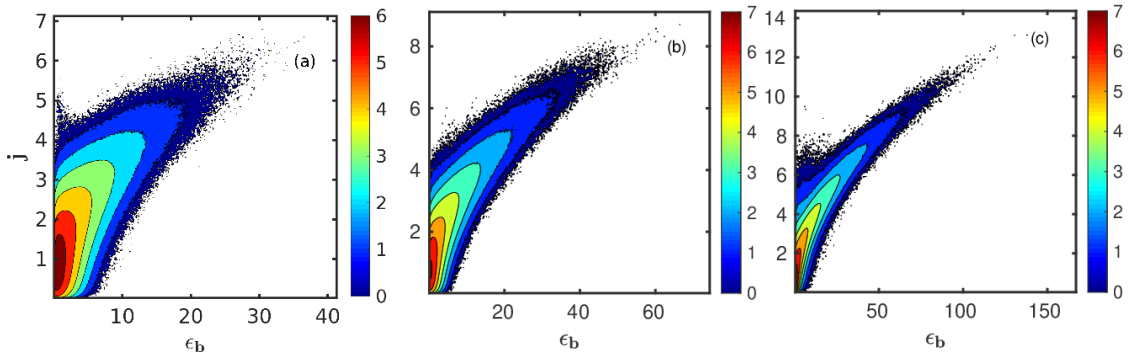


**Figure 34.** Joint PDF of  $j$  and  $\epsilon_b$  for 3DRFMHD shown as filled contour plots on a logarithmic scale for (a)  $\text{Pr}_M = 0.1$ , (b)  $\text{Pr}_M = 1$ , and (c)  $\text{Pr}_M = 10$ . The arguments of the joint PDFs are normalized by their mean values.

Joint PDFs of  $\omega$  and  $\epsilon_u$  are shown in Figs. 33 and those for  $j$  and  $\epsilon_b$  in figures 34 for (a)  $\text{Pr}_M = 0.1$ , (b)  $\text{Pr}_M = 1$ , and (c)  $\text{Pr}_M = 10$  for 3DRFMHD.

#### 4. Discussions

We have carried out a detailed study of 3DRFMHD turbulence. Our study has been designed specifically to study the systematics of the dependence of these properties on the magnetic Prandtl number  $\text{Pr}_M$  and to compare them with their counterparts in 3DMHD turbulence. Our study is restricted to incompressible MHD turbulence; we do not include a mean magnetic field as, e.g., in Refs. [54]; furthermore we do not study Lagrangian properties considered, e.g., in Ref. [55]. In our studies we obtain (a) various PDFs, such as those of  $\omega$ ,  $j$ , the energy dissipation rates, of the cosines of angles between various vectors, and scale-dependent velocity and magnetic-field increments, (b) spectra, e.g., those of the energy and the effective pressure, (c) velocity and magnetic-field structure functions that can be used to characterize small-length-scale intermittency, (d) isosurfaces of quantities such as  $\omega$  and  $j$ , and (e) joint PDFs such as  $QR$  plots. The evolution of these properties with  $\text{Pr}_M$  has been described in detail in the previous Section.

Such a comprehensive study of 3DRFMHD turbulence has not been attempted heretofore. All earlier studies have concentrated on field-theoretical studies of correlation functions and spectra in 3DRFMHD; typically these studies use Fourier-space renormalization group methods, at one- or two-loop levels, or closures that concentrate on K41-type scaling results [37]. One of these studies [63] has suggested, that multiscaling exponents might depend on the cross correlations between the random forces in 3DRFMHD.

Here we wish to highlight, and examine in detail, the implications of our study for intermittency. Some earlier DNS studies, such as Refs. [26, 64], had noted that, for the case  $\text{Pr}_M = 1$ , the magnetic field is more intermittent than the velocity field. This is why we have concentrated on velocity and magnetic-field structure functions. Our 3DRFMHD study confirms this finding, for the case  $\text{Pr}_M = 1$ , as can be seen clearly from the comparison of our exponent ratios, for  $\text{Pr}_M = 1$ , with those of the recent DNS studies of 3DMHD turbulence [26, 32, 33]. The error bars that we quote for our exponent ratios have been calculated as described in the previous Section. Thus, at least given our error bars, there is agreement between our 3DRFMHD exponent ratios with those of 3DMHD [32, 33]. However, these error bars are large, so a decisive comparison of multiscaling exponent ratios of 3DRFMHD and 3DMHD turbulence must await higher-resolution DNS studies than those presented here. The  $\text{Pr}_M$  dependence of these exponent ratios is also similar for 3DRFMHD and 3DMHD turbulence.

Recent experimental studies of MHD turbulence in the solar wind [16, 17] provide evidence for velocity fields that are more strongly intermittent than the magnetic field; this study does not give the value of  $\text{Pr}_M$ . However, their data for multiscaling exponents are qualitatively similar to those we obtain at low values of  $\text{Pr}_M$ . Of course, we must exercise caution in comparing results from DNS studies of homogeneous, isotropic, incompressible MHD turbulence with measurements on the solar wind in which anisotropy, compressibility, and kinetic effects can be significant.

Moreover, we address the issue of universality of exponent ratios in 3DMHD and 3DRFMHD turbulence. This is of central importance in deciding whether we can defensibly use the latter as a model for obtaining universal statistical properties, such as exponent ratios, by employing field-theoretic renormalization-group methods. At the level of the DNS study we have presented here for 3DRFMHD, these exponent ratios for 3DRFMHD and 3DMHD seem to agree, given our large error bars, in all except a few cases (e.g., order  $p = 1$  and  $\text{Pr}_M = 1$ ) [32, 33] even though some PDFs are different in detail and isosurfaces of  $\omega$ ,  $j$ , etc., are qualitatively different. Of course, as we have mentioned above, strictly speaking 3DMHD and 3DRFMHD turbulence cannot be in the same universality class because of logarithmic corrections to, say,  $E(k)$  that arise from the power law in the random forcing we employ. Such logarithmic corrections have been discussed in the analogous randomly forced versions of the 3D Navier-Stokes equation [51] and the 1D Burgers equation [50].

## Acknowledgements

GS thanks AtMath Collaboration at the University of Helsinki. We thank D. Mitra, S.S. Ray and A.K. Verma for discussions, SERC(IISc) for computational resources and DST, UGC and CSIR India for support.

Author contributions: GS, AB, and RP planned the study; GS and NBP carried out the numerical simulations; NBP, GS, and RP analyzed the results; NBP, GS, and RP wrote the manuscript; All authors checked and approved the final version of the manuscript.

## References

- [1] U. Frisch, *Turbulence: The Legacy of A.N. Kolmogorov* (Cambridge University, Cambridge, England, 1996).
- [2] R. Pandit, P. Perlekar, S.S. Ray, *Pramana* **73**, 157 (2009).
- [3] A. R. Choudhuri, *The Physics of Fluids and Plasmas: An Introduction for Astrophysicists* (Cambridge University Press, Cambridge, UK, 1998).
- [4] V. Krishan, *Astrophysical plasmas and fluids* (Kluwer Academic Publishers, Netherlands, 1999).
- [5] G. Rüdiger and R. Hollerbach, *The Magnetic Universe: Geophysical and Astrophysical Dynamo Theory* (Wiley, Weinheim, 2004).
- [6] H. Goedbloed and S. Poedts, *Principles of Magnetohydrodynamics With Applications to Laboratory and Astrophysical Plasmas* (Cambridge University Press, Cambridge, UK, 2004).
- [7] D. Biskamp, *Magnetohydrodynamic Turbulence* (Cambridge University Press, Cambridge, UK, 2003).
- [8] M.K. Verma, *Phys. Rep.* **441**, 229 (2004).
- [9] E. Dormy and J.-L. Le Mouél, *C.R. Physique* **9**, 711 (2008).
- [10] P. H. Roberts and G. A. Glatzmaier, *Rev. Mod. Phys.* **72**, 1081 (2000).
- [11] F. Pétrélis and S. Fauve, *Europhys. Lett.* **22**, 273 (2001); **76**, 602 (2006); S. Fauve and F. Pétrélis, in *Peyresq Lectures on Nonlinear Phenomena*, edited by J.-A. Sepulchre (World Scientific, Singapore, 2003), Vol. 2, pp. 1-64; S. Fauve, F. Pétrélis, *C.R. Physique* **8**, 87 (2007).
- [12] A. Gailitis *et al.*, *Phys. Rev. Lett.* **84**, 4365 (2000); *Phys. Rev. Lett.* **86**, 3024 (2001); *Rev. Mod. Phys.* **74**, 973 (2002); *Surv. Geophys.* **24**, 247 (2003); *Phys. Plasmas* **11**, 2838 (2004).

- [13] R. Stieglitz and U. Müller, *Phys. Fluids* **13**, 561 (2001); U. Müller and R. Stieglitz, *Nonlin. Proc. Geophys.* **9**, 165 (2002); U. Müller, R. Stieglitz, and S. Horanyi, *J. Fluid Mech.* **498**, 31 (2004).
- [14] N. L. Peffley, A. B. Cawthorne, and D. P. Lathrop, *Phys. Rev. E* **61**, 5287 (2000); W.L. Shew and D.P. Lathrop, *Phys. Earth Planet. Inter.* **153**, 136 (2005).
- [15] M. Bourgoin *et al.*, *Phys. Fluids* **14**, 3046 (2002); **16**, 2529 (2004); L. Marié *et al.*, *Magnetohydrodynamics* **38**, 163 (2002); R. Monchaux *et al.*, *Phys. Rev. Lett.* **98**, 044502 (2007).
- [16] C. Salem, A. Mangeney, S. D. Bale, and P. Veltri, *Astrophys. J.*, **702**, 537 (2009).
- [17] J. J. Podesta, D. A. Roberts, and M. L. Goldstein, *Astrophys. J.* **664**, 543 (2007); J. J. Podesta, B. D. G. Chandran, A. Bhattacharjee, D. A. Roberts and M. L. Goldstein, *J. Geophys. Res.* **114**, A01107 (2009).
- [18] A.A. Schekochihin, *et al.*, *Phys. Rev. Lett.*, **92**, 054502 (2004).
- [19] B. G. Elmegreen and J. Scalo, *Annual Rev. of Astronomy and Astrophys.* **42**, 211 (2004).
- [20] Y. Ponty, P. D. Mininni, D. C. Montgomery, J.-F. Pinton, H. Politano, and A. Pouquet, *Phys. Rev. Lett.* **94**, 164502 (2005).
- [21] A. N. Kolmogorov, *Dokl. Akad. Nauk. SSSR* **30**, 9 (1941); **32**, 16 (1941); *Proc. R. Soc. London, Ser. A* **434**, 9 (1991); **434**, 15 (1991); *C. R. Acad. Sci. USSR* **30**, 301 (1941).
- [22] C. Kalelkar and R. Pandit, *Phys. Rev. E* **69**, 046304 (2004).
- [23] P. D. Mininni, A. G. Pouquet, and D. C. Montgomery, *Phys. Rev. Lett.* **97**, 244503 (2006).
- [24] J. Mason, F. Cattaneo, and S. Boldyrev, *Phys. Rev. E* **77**, 036403 (2008).
- [25] J. Baerenzung, H. Politano, Y. Ponty, and A. Pouquet, *Phys. Rev. E* **77**, 046303 (2008); **78**, 026310 (2008).
- [26] P. D. Mininni and A. Pouquet, *Phys. Rev. E* **80**, 025401 (2009).
- [27] W-C. Müller and D. Biskamp, *Phys. Rev. Lett.* **84**, 475 (2000); *Phys. Rev. E* **67**, 066302 (2003).
- [28] V. Dallas, and A. Alexakis, *Phys. Fluids* **25**, 105106 (2013).
- [29] D. Biskamp, and W.C. Müller, *Physics of Plasmas* **7**, 4889 (2000).
- [30] Y. Ponty, J. P. Laval, B. Dubrulle, F. Daviaud, and J.-F. Pinton, *Phys. Rev. Lett.* **99**, 224501 (2007); *C. R. Acad. Sci. (Paris)* **9**, 749 (2008).
- [31] A. Brandenburg, *Astrophys. J.* **697**, 1206 (2009).
- [32] G. Sahoo, P. Perlekar, and R. Pandit, *New J. Phys.***13**, 013036 (2011).
- [33] G. Sahoo, *PhD Thesis*(unpublished), (Indian Institute of Science, India, 2010).
- [34] C. DeDominicis and P.C. Martin, *Phys. Rev. A* **19**, 419 (1979).
- [35] V. Yakhot and S.A. Orszag, *J. Sci. Comput.* **1**, 3 (1986); W.P. Dannevik, V. Yakhot, and S.A. Orszag, *Phys. Fluids* **30**, 2021 (1987).
- [36] J.K. Bhattacharjee, *J. Phys. A* **21**, L551 (1988).
- [37] L. Ts Adzhemyan, N.V. Antonov, A.N. Vasiliev, *Field Theoretic Renormalization Group in Fully Developed Turbulence* (Gordon and Breach, Amsterdam, 1999).
- [38] J. Busa, M. Hnatich, J. Honkonen, and D. Horvath, *Phys. Rev. E* **55**, 381 (1997)
- [39] P. Olla, *Phys. Rev. Lett.* **67**, 2465 (1991).
- [40] J.-D Fournier , P.-L Sulem, and A. Pouquet, *J. Phys. A: Math. Gen.* **15**, 1393 (1982).
- [41] L.Ts. Adzhemyan, A.N. Vasil'ev, and M. Hnatich, *Teoreticheskayai Matematicheskaya Fizika* **64**, 196 (1985); L.Ts. Adzhemyan, J. Honkonen, M.V. Kompaniets, A.N. Vasil'ev, *Phys. Rev. E* **71**, 036305 (2005).
- [42] M. Hnatic, D. Horvath, R. Semancik, and M. Stehlik, *Czech. J. Phys.* **45**, 91 (1995).
- [43] M. Hnatic, J. Honkonen, and M. Jurcisin, *Phys. Rev. E* **64**, 056411 (2001).
- [44] C.B. Kim, *Physics of Plasmas* **11**, 934 (2004).
- [45] C.B. Kim, and T.J. Yang, *Physics of Plasmas* **6**, 2714 (1999).
- [46] Y. Zhou and G. Vahala, *J. Plasma Phys.* **39**, 511 (1988).
- [47] Y. Zhou, *Elsevier* **488**, 1-49 (2010).
- [48] A. Chekhlov and V. Yakhot, *Phys. Rev. E* **51**, 2739 (1995).
- [49] F. Hayot and C. Jayaprakash, *Phys. Rev. E* **54**, 4681 (1996).
- [50] D. Mitra, J. Bec, R. Pandit and U. Frisch, *Phys. Rev. Lett.* **94**, 194501 (2005).

- [51] A. Sain, Manu and R. Pandit, Phys. Rev. Lett. **81**, 4377 (1998).
- [52] L. Biferale, M. Cencini, A.S. Lanotte, M. Sbragaglia, and F. Toschi, New J. Phys. **6** 37 (2004).
- [53] A. Mazzino, P. Muratore-Ginanneschi, and S. Mussachio, J. Stat. Mech. **10**, P10012 (2009).
- [54] P. Goldreich and S. Sridhar, Astrophys. J. **438**, 763 (1995).
- [55] For representative Lagrangian studies of MHD turbulence see H. Homann, R. Grauer, A. Busse and W. C. Müller, J. Plasma Phys. **73**, 821 (2007).
- [56] C. Canuto, M.Y. Hussaini, A. Quarteroni and T.A. Zang, *Spectral Methods in Fluid Dynamics* (Springer, Berlin, 1988); *Spectral Methods Evolution to Complex Geometries and Applications to Fluid Dynamics* (Springer, Berlin, 2007).
- [57] B. J. Cantwell, Phys. Fluids A **5**, 2008 (1993).
- [58] P.A. Davidson, *Turbulence* (Oxford University Press, Oxford, 2004).
- [59] L. Biferale, L. Chevillard, C. Meneveau, and F. Toschi, Phys. Rev. Lett. **98**, 214501 (2007).
- [60] P. Iroshnikov, Astron. Zh. **40**, 742 (1963); R. H. Kraichnan, Phys. Fluids **8**, 1385 (1965).
- [61] R. Benzi, S. Ciliberto, R. Tripicciono, C. Baudet, F. Massaioli, and S. Succi, Phys. Rev. E **48**, R29 (1993).
- [62] S. Chakraborty, U. Frisch, and S. S. Ray, J. Fluid Mech., **649**, 275 (2010).
- [63] A. Basu, Europhys. Lett. **65**, 505 (2004).
- [64] A. Basu, A. Sain, S.K. Dhar and R. Pandit, Phys. Rev. Lett. **81**, 2687 (1998).
- [65] M.K. Verma, Phys. Plasmas **6**, 1455 (1999).
- [66] M. Bourgoin *et al.*, Phys. Fluids **14**, 3046 (2002); R. Monchaux *et al.*, Phys. Rev. Lett. **98**, 044502 (2007).
- [67] S. Boldyrev, Phys. Rev. Lett. **96**, 115002 (2006); S. Boldyrev, J. Mason, and F. Cattaneo, Astrophys. J. **699** L39 (2009).
- [68] W.D. McComb, *The Physics of Fluid Turbulence* (Clarendon, Oxford, 1990).
- [69] C.-Y. Mou and P.B. Weichman, Phys. Rev. E, **52**, 3738 (1995).
- [70] G.L. Eyink, Phys. Fluids **6**, 3063 (1994).
- [71] L.L. Kichatinov, Magnetohydrodynamics **21**, 105 (1985).
- [72] R.G. Kleva, Phys. Fluids **29**, 2882 (1986).
- [73] D.W. Longcope and R.N. Sudan, Phys. Fluids B **3**, 1945 (1991).
- [74] S.J. Camargo and H. Tasso, Phys. Fluids B **4**, 1199 (1992).
- [75] M.K. Verma and J.K. Bhattacharjee, Europhys. Lett. **31**, 195 (1995).
- [76] C.C. Chang and B.S. Lin, J. Phys. Soc. Jpn. **71**, 1450 (2002).
- [77] S. Servidio, W. H. Matthaeus, and P. Dmitruk, Phys. Rev. Lett. **100**, 095005(2008).